~~CAPS v1.0:~~ An improved regional coupled modeling system for Arctic sea ice ~~and climate~~ simulation and prediction: a case study for 2018

Chao-Yuan Yang[1], Jiping Liu[2], Dake Chen[1]

[1]School of Atmospheric Sciences, Sun Yat-sen University, and Southern Marine Science and Engineering Guangdong Laboratory (Zhuhai), Zhuhai, Guangdong, China

[2]Department of Atmospheric and Environmental Sciences, University at Albany, State University of New York, Albany, NY, USA

Corresponding author:

Chao-Yuan Yang (yangchy36@mail.sysu.eu.cn) and Jiping Liu (jliu26@albany.edu)

Abstract

The improved/updated Coupled Arctic Prediction System (CAPS) is evaluated by a set of Pan-Arctic prediction experiments for the year 2018, which is built on ~~new versions of~~ Weather Research and Forecasting model (WRF), the Regional Ocean Modeling System (ROMS), the Community Ice CodE (CICE), and a data assimilation based on the Local Error Subspace Transform Kalman Filter. ~~A set of Pan-Arctic prediction experiments with~~We analyze physical process linking improved/changed physical parameterizations in WRF, ROMS, and CICE ~~as well as different configurations are performed for~~ to changes in the ~~year 2018 to assess their impacts on the predictive skill of~~simulated Arctic sea ice ~~at seasonal timescale. The key improvements of WRF, including cumulus,~~ state. Our results show that the improved convection and boundary layer~~, and land surface~~ schemes~~,~~ in WRF result in improved simulation in downward radiative fluxes and near surface air temperature ~~and downward radiation. The major changes of ROMS, including~~, which influences the predicted ice thickness. The changed tracer advection and vertical mixing schemes~~, lead~~ in ROMS reduces the bias in sea surface temperature and changes ocean temperature and salinity structure in the surface layer, leading to improved evolution of the predicted ~~total~~ ice extent (particularly correcting the late ice recovery issue in the previous CAPS~~), and reduced biases in sea surface temperature.~~). The ~~changes of CICE, that include~~ improved sea ice thermodynamics ~~and assimilation of new sea ice thickness product,~~in CICE have noticeable influences on the predicted ice thickness ~~and the timing of ice recovery. Results from the prediction experiments suggest that the updated~~. The updated CAPS can better predict the evolution of ~~total ice~~

~~extent~~Arctic sea ice during the melting season compared with its predecessor, though the ~~predictions~~prediction still have ~~certain~~some biases at the regional scale. We further show that the updated CAPS can remain skillful beyond the melting season, which may have potential values for stakeholders making decisions for socioeconomical activities in the Arctic.

1. Introduction

Over the past few decades, the extent of Arctic sea ice has decreased rapidly and entered a thinner/younger regime associated with global climate change (e.g., Kwok, 2018; Serreze and Meier, 2019). The ~~drastic~~dramatic changes in the properties of Arctic sea ice have ~~captured~~gained increasing attentions ~~of~~by a wide range of stakeholders, such as trans-Arctic shipping, natural resource exploration, and activities of coastal communities relying on sea ice (e.g., Newton et al., 2016). This leads to increasing demands on skillful Arctic sea ice prediction, particularly at seasonal timescale (e.g., Jung et al., 2016; Liu et al., 2019; Stroeve et al., 2014). However, Arctic sea ice prediction based on different approaches (e.g., statistical method and dynamical model) submitted to the Sea Ice Outlook, a community effort managed by the Sea Ice Prediction Network (SPIN, https://www.arcus.org/sipn), shows substantial biases in the predicted seasonal minimum of Arctic sea ice extent compared to the observations for most years since 2008 (Liu et al., 2019; Stroeve et al., 2014).

Recently, we have developed an atmosphere-ocean-sea ice regional coupled modeling system, for seasonal Arctic sea ice and climate prediction (Yang et al., 2020, hereafter Y20), in which the Los Alamos Sea Ice Model (CICE) is coupled with the Weather Research and Forecasting Model (WRF) and the Regional Ocean Modeling System (ROMS), hereafter called Coupled Arctic Prediction System (CAPS). To improve the accuracy of initial sea ice conditions, CAPS employs an ensemble-based data assimilation system to assimilate satellite-based sea ice observations. Seasonal Pan-Arctic sea ice predictions with improved initial sea ice conditions conducted in Y20 have shown that CAPS has the potential to provide skillful

Arctic sea ice prediction at seasonal timescale.

We know that the changes of sea ice variables (e.g., ice extent, ice concentration, ice thickness, ice drift) are mainly driven by forcings from the atmosphere and the ocean. Atmospheric cloudiness and related radiation influence surface ice melting (Huang et al., 2019; Kapsch et al., 2016; Kay et al., 2008) and the energy stored in the surface mixed layer that determines the seasonal ice melt and growth (e.g., Perovich et al., 2011, 2014). Atmospheric circulation is the primary driver for the transportation of sea ice and partly responsible for the variability of Arctic sea ice (e.g., Mallett et al., 2021; Ogi et al., 2010; Zhang et al., 2008). Olonscheck et al. (2019) suggested that atmospheric temperature fluctuations explain a majority of Arctic sea ice variability while other drivers (e.g., surface winds, and poleward heat transport) account for about 25% of Arctic sea ice variability. The oceanic heat inputs (as well as salt inputs) into the Arctic Ocean include the Atlantic Water (AW; Aagaard, 1989; McLaughlin et al., 2009) through the Barents Sea, and the Pacific Water (PW; Itoh et al., 2013; Woodgate et al., 2005) from the Bering Strait. The oceanic heat inputs from AW and PW are not directly available for sea ice since they are separated from a cold and fresh layer underlying sea ice (e.g., Carmack et al., 2015, Fig. 2). Vertical mixing by the internal wave (e.g., Fer, 2014) and double diffusion (e.g., Padman and Dillon, 1987; Turner, 1973) are the principal processes for upward heat transport from the subsurface layer (i.e., AW and PW) to the surface mixed layer in the Arctic Ocean. Sea ice thermodynamics determines how thermal properties of sea ice (e.g., temperature, salinity) change. These changes then influence the thermal structure of underlying ocean through interfacial fluxes (i.e., heat, salt and freshwater fluxes; DuVivier et al., 2021; Kirkman IV and Bitz, 2011) and ice thickness (e.g., Bailey et al., ~~The skills of coupled climate models (GCMs) in predicting Pan-Arctic sea ice extent have been assessed with suites of hindcasts, and these studies suggested that GCMs have skill in predicting ice extent~~2020).

The CAPS is configured for the Arctic with sufficient flexibility. That means each model component of CAPS (WRF, ROMS, and CICE) has different physics options for us to choose and capability to integrate ongoing improvements in physical parameterizations. Recently, the WRF model has adapted improved convection and boundary layer schemes in the Rapid Refresh (RAP) model operational at the National Centers for Environmental Prediction (NCEP, Benjamin et al., 2016). The first question we want to answer in this paper is to what extent these modifications can improve atmospheric simulations in the Arctic (i.e., radiation, temperature, humidity, and wind), and then benefit seasonal Arctic sea ice simulation and prediction. The ROMS model provides several options for tracer advection schemes. These advection schemes can have different degrees of oscillatory behavior (e.g., Shchepetkin and McWilliams, 1998). The oscillatory behavior can have impacts on sea ice simulation through ice-ocean interactions (e.g., Naughten et al., 2017). The second question we want to answer in this paper is to what extent different advection schemes can change the simulation of upper ocean thermal structure and then Arctic sea ice prediction. Several recent efforts have incorporated prognostic salinity into sea ice models. The CICE model has a new mushy-layer thermodynamics parameterization that includes prognostic salinity and treats sea ice as a two-phase mushy layer (Turner et al., 2013). Bailey et al. (2020) showed that the mushy-layer physics has noticeable impacts on Arctic sea ice simulation within the Community Earth

System Model version 2. The third question we want to answer in this paper is whether the mushy-layer scheme can produce noticeable influence on seasonal Arctic sea ice prediction. Currently, SIPN focuses on Arctic sea ice predictions during the melting season, particularly seasonal minimum. It is not clear that how predictive skills of dynamical models participating in SIPN may change for longer period, i.e., extending into the freezing up period, which also have significance on socioeconomic aspects. The assessment of the skills of global climate models (GCMs) in predicting Pan-Arctic sea ice extent with suites of hindcasts suggested that GCMs may have skill at lead times of 1-6 months (e.g., Blanchard-Wrigglesworth et al., 2015; Chevallier et al., 2013; Guemas et al., 2016; Merryfield et al., 2013; Msadek et al., 2014; Peterson et al., 2015; Sigmond et al., 2013; Wang et al., 2013; Zampieri et al., 2018). Moreover, some studies using a "perfect model" approach, which ~~examines~~treats one member of an ensemble as the truth (i.e., assuming the model is prefect without bias) and analyzes the skill of ~~a model~~ other members in predicting ~~itself,~~the response of the "truth" member (e.g., Meehl et al., 2007), suggested that Arctic sea ice cover can be potentially predictable up to two years in advance (e.g., Blanchard-Wrigglesworth et al., 2011; Blanchard-Wrigglesworth and Bushuk, 2018; Day et al., 2016; Germe et al., 2014; Tietsche et al., ~~2014). The gap between actual predictive skill with dynamical models and theoretical predictability suggested by "perfect model" studies may be related to inaccurate initial conditions and/or inadequate physical parameterizations in dynamical models (Stroeve et al., 2015~~2014). The last question we want to answer in this paper is whether CAPS has predictive skill for longer periods (up to 7 months).

~~Recently, we have developed an atmosphere-ocean-sea ice regional coupled modeling~~

~~system, hereafter called Coupled Arctic Prediction System (CAPS), for seasonal Arctic sea ice and climate prediction (Yang et al., 2020, hereafter Y20). To improve the accuracy of initial sea ice conditions, CAPS employs an ensemble-based data assimilation system to assimilate satellite-based sea ice observations. Seasonal Pan-Arctic sea ice predictions with improved initial sea ice conditions conducted in Y20 have shown that CAPS has potential to provide skillful Arctic sea ice predictions at seasonal timescale.~~

~~With recent improvements in the model components of CAPS, this paper gives a description of the updated CAPS, and presents the assessment of seasonal Arctic sea ice predictions associated with improved/changed physical parameterizations.~~ This paper is structured as follows. Section 2 provides ~~an~~a brief overview of ~~the~~ CAPS, including ~~major changes/improvements in the~~ model ~~components compared to its predecessor described in Y20, as well as the~~ configurations and data assimilation ~~system and the assimilation~~ procedures. Section 3 describes the designs of the prediction experiments~~, and~~ for the year of 2018 based on major improvements/ changes in the model components compared to its predecessor described in Y20, examines the performance of the updated CAPS~~ associated with major~~, and offers physical links between Arctic sea ice changes~~/improvements in the model components. Some discussions~~ and improved/changed physical parameterizations. Section 4 discusses the predictive skill of CAPS at longer timescale. Discussions and concluding remarks ~~and~~ are given in section ~~4 and~~ 5.

2. Coupled Arctic Prediction System (CAPS)

As described in Y20, ~~to enhance our ability to predict seasonal Arctic sea ice as well as~~

~~climate, we have developed CAPS~~the CAPS has been developed by coupling the Community Ice CodE (CICE) with the Weather Research and Forecasting Model (WRF) and the Regional Ocean Modeling System (ROMS) based on the framework of the Coupled Ocean-Atmosphere-Wave-Sediment Transport (~~COAWST) modeling framework (~~Warner et al., 2010). The general description of each model component in CAPS is referred to Y20. The advantage of CAPS is its model components have ~~different~~a variety of physics ~~options~~ for us to choose~~.~~ and capability to integrate follow-up improvements of physical parameterizations. With recent achievements of community efforts~~ on improving the WRF, ROMS, and CICE models, in this study~~, we update CAPS based on newly-released WRF, ROMS, and CICE models~~ for further development of our Arctic sea ice~~. During this update, we focus on the Rapid Refresh (RAP) physics in the WRF model, the oceanic tracer advection scheme in the ROMS model, sea ice thermodynamics in the CICE model (see details in section 3), and investigate physical process linking them to Arctic sea ice simulation and prediction~~ system. Table 1 provides the versions for these model components between this paper and Y20.~~. The same physical parameterizations described in Y20 are used here for the control simulation~~, but some of them are improved as the WRF, ROMS, and CICE models released their new versions (see Table 2).~~ (see Table 1). Major changes in ~~physics parameterization and~~ physical parameterizations as well as the model infrastructure in the WRF, ROMS, and CICE models are described ~~below.~~

~~**2.1. Model components and updates**~~

~~WRF: The WRF model (Skamarock et al., 2005) is a non-hydrostatic and quasi-compressible model, which uses hybrid vertical coordinate with the top of the model at 50 mb~~

~~and the Arakawa C-grid in horizontal. The Rapid Refresh (RAP) system, a high-frequency, continental-scale weather prediction/assimilation modeling system operational at the National Centers for Environmental Prediction (NCEP), has made some improvements in the WRF model physics (Benjamin et al., 2016). The official release of WRF model since version 3.9 has adapted these modified physics parameterizations in the RAP system, including the Grell-Freitas convection scheme (GF) and the Mellor-Yamada-Nakanishi-Niino planetary boundary layer (PBL) scheme (MYNN) as the replacement of original schemes in the WRF model. For the GF scheme, the major improvements compared to the original scheme (Grell and Freitas, 2014) include: 1) a beta probability density function used as the normalized mass flux profile for representing height-dependent entrainment/detrainment rates within statistical-averaged deep convective plumes, and 2) the European Centre for Medium-Range Weather Forecasts (ECMWF) approach used for momentum transport due to convection (Biswas et al.~~ in section~~2020; Freitas et al. 2018). For the MYNN scheme, compared to the original scheme (Nakanishi and Nino, 2009), the RAP system improved the mixing-length formulation and removed numerical deficiencies to better represent subgrid-scale cloudiness (Benjamin et al. 2016, see Append. B).~~

~~For the Noah land surface model (Chen and Dudhia, 2001), some issues including discontinuous behavior for soil ice melting and negative moisture fluxes over glacial and sea ice, as well as minor issues associated with snow melting have been fixed since the release of WRF version~~ 3.~~9.~~

~~ROMS: The ROMS model is a terrain-following and free-surface model, which solves~~

~~three-dimensional Reynolds-averaged Navier-Stokes equations with the hydrostatic and Boussinesq approximation (Shchepetkin and McWilliams, 2005; Haidvogel et al., 2008). In the vertical, the equations are discretized over bottom topography with stretching terrain-following coordinates (Song and Haidvodel, 1994). In the horizontal, the ROMS model uses boundary-fitted, orthogonal curvilinear coordinates on a staggered Arakawa C-grid. In the updated CAPS, the major change in the latest ROMS model is associated with surface heat/freshwater fluxes and their coupling to other model components. This change prevents the potentially erroneous results when the ROMS timestep is smaller than the coupling frequency with other model components. Other changes in the ROMS model of the updated CAPS can be found in the ROMS distribution website (https://www.myroms.org/projects/src/report/4 Ticket #654 to #824).~~

~~CICE: The CICE model is designed to be a sea ice model component for global coupled climate models. Its dynamic core simulates the movement of sea ice based on forces from the atmosphere, the ocean, and Earth's rotation and the material strength of the ice. The new feature of CICE version 6.0.0 contains an independent software package, Icepack, to provide the column physics code for all thermodynamic parameterizations in a single grid cell. These parameterizations include the MUSHY-layer ice thermodynamics (Turner et al., 2013) that resolves prognostic vertical temperature and salinity profiles. The new version of CICE also includes improvements in sea ice rheology and a new landfast-ice parameterization (Lemieux et al., 2016). More details can be found in the CICE Consortium GitHub page (https://github.com/CICE-Consortium).~~

~~2.2. Data Assimilation and evaluation data~~

As described in Y20, the Parallel Data Assimilation Framework (PDAF, Nerger and Hiller, 2013) was implemented in CAPS~~ for assimilating sea ice observations~~, which provides a variety of optimized ensemble-based Kalman filters~~ including the Local Ensemble Transform Kalman Filter (LETKF; Hunt et al., 2007), the Localized Singular Evolutive Interpolated Kalman (LSEIK; Nerger et al., 2006), and the~~. The Local Error Subspace Transform Kalman Filter (LESTKF; Nerger et al., 2012~~). Following Y20, the LESTKF~~) is used to assimilate satellite-observed sea ice parameters. The LESTKF projects the ensemble onto the error subspace and then directly computes the ensemble transformation in the error subspace. This results in better assimilation performance ~~compared to the LSEIK filter~~ and higher computational efficiency compared to the ~~LETKF~~other filters as discussed in Nerger et al. (2012).

The initial ensembles are generated by applying the second-order exact sampling (Pham, 2001) to simulated sea ice state vectors (ice concentration and thickness) from an one-month free run, and then assimilating sea ice observations~~ that include~~, including: 1) the near real-time daily Arctic sea ice concentration processed by the National Aeronautics and Space Administration (NASA) Team algorithm (Maslanik and Stroeve, 1999) obtained from the ~~National Snow and Ice Data Center (~~NSIDC~~;~~ (https://nsidc.org/data/NSIDC-0081/), and 2) a combined monthly sea ice thickness derived from the CryoSat-2 (Laxon et al., 2013; obtained from http://data.seaiceportal.de), and daily sea ice thickness derived from the Soil Moisture and Ocean Salinity (SMOS; Kaleschke et al., 2012; Tian-Kunze et al., 2014; obtained from https://icdc.cen.uni-hamburg.de/en/l3c-smos-sit.html). To address the issue that sea ice thickness derived from CyroSat-2 and SMOS are unavailable during the melting season, the melting season ice thickness is estimated based on the seasonal cycle of the Pan-Arctic Ice Ocean Modeling and Assimilation System (PIOMAS) daily sea ice thickness (Zhang and Rothrock, 2003~~) as described in Y20.~~).

~~In~~ Different from Y20, in this study, ~~compared with Y20,~~ we change the localization radius from 2 to 6 grids during the assimilation procedures~~. The sea ice component in the updated CAPS experienced~~ to reduce some instability ~~at~~during initial Arctic sea ice simulations associated with 2 localization radii. As shown in Supplementary Figure S1, the ice thickness with 2 localization radii ~~but not with 6 localization radii. Figure 1 shows that initial sea ice thickness after the data assimilation with (a) 2 localization radii~~ and 1.5 m uncertainty ~~for assimilating ice thickness and (b) 6 localization radii and 0.75 m uncertainty. The initial ice thickness for both configurations has similar spatial distribution. However, the ice thickness with 2 localization radii and 1.5 m uncertainty shows~~ (used in Y20) shows some discontinuous features (Fig. ~~1a~~S1a), which ~~results~~tends to result in numerical instability during the initial ~~model~~ integration. Such discontinuous ~~feature is~~features are obviously corrected with 6 localization radii and 0.75 m uncertainty (Fig. ~~1b~~S1b). Following Y20, here we test the 2018 prediction experiment with ~~2 and~~ 6 localization radii ~~but the same uncertainty for ice thickness (0.75m)~~ for the data assimilation ~~(Y20 and Y20_MOD, see Table 3). The Y20 and Y20_MOD experiments show~~, which shows very similar temporal ~~evolutions~~evolution of the total Arctic sea ice extent for the July experiment relative to that of Y20, although ~~Y20_MOD~~it (red solid line) predicts slightly less ice extent than that of Y20 (blue line) ~~for the July experiment~~ ~~(~~(Supplementary Figure ~~2~~S2). In this study, ~~the~~this configuration ~~of Y20_MOD~~ is designated as the reference for the following assessment of the updated CAPS~~.~~ (hereafter Y20_MOD).

For the evaluation of Arctic sea ice prediction, Sea Ice Index (Fetterer et al., 2017; obtained from https://nsidc.org/data/G02135) is used as the observed total sea ice extent, and the NSIDC sea ice concentrations (SIC) derived from Special Sensor Microwave Imager/Sounder (SSMIS) with the NASA Team algorithm (Cavalieri et al., 1996; obtained from https://nsidc.org/data/nsidc-0051) is ~~employed~~also used. For the assessment of the simulated atmospheric and oceanic variables, the ECMWF reanalysis version 5 (ERA5; Hersbach et al., 2020; obtained from https://cds.climate.copernicus.eu) and National Oceanic and Atmospheric Administration (NOAA) Optimum Interpolation (OI) Sea Surface Temperature (SST) (Reynolds et al., 2007; obtained from https://psl.noaa.gov/data/gridded/data.noaa.oisst.v2.highres.html) are utilized. For the comparison of spatial distribution, SIC, ERA5, and OISST are interpolated to the model grid.

3. ~~Model~~ Evaluation of updated CAPS

3.1. Experiment designs and methodology

~~Following Y20, the~~The model domain includes 319 (449) x- (y-) grid points with a ~24 km grid spacing for all model components (see Figure 2 in Y20). The WRF model uses 50 vertical levels, the ROMS model uses 40 vertical levels, and the CICE model uses 7 ice layers, 1 snow layer, and 5 categories of sea ice thickness. The coupling frequency across all model components is 30 minutes. Initial and boundary conditions for the WRF and ROMS models are generated from the Climate Forecast System version 2 (CFSv2, Saha et al., 2014) operational forecast archived at NCEP (http://nomads.ncep.noaa.gov/pub/data/nccf/com/cfs/prod/). Sea ice initial conditions are generated from the data assimilation described in section 2.~~2.~~ Ensemble predictions with 8 members are conducted. A set of numerical experiments for the Pan-Arctic seasonal sea ice prediction with different ~~configurations~~physics, starting from July 1st to October 1st for the year of 2018, has been conducted. Table ~~3~~2 provides the details of these experiments that allow us to examine ~~impacts of~~physical process linking improved/changed physical parameterizations in the updated CAPS ~~on~~to Arctic sea ice simulation and prediction ~~at seasonal timescale~~.

~~3.2.3.1.~~ In this study, sea ice extent ~~Impacts of the RAP physics in the WRF model~~

~~To examine the performance the updated CAPS compared to its predecessor in Y20, the Y21_CTRL experiment uses some updated physics configurations in the WRF model as listed in Table 2. The temporal evolution of the ensemble mean of the predicted Arctic sea ice extent for the Y21_CTRL and Y20_MOD experiments along with the NSIDC observations are shown in Figure 3. The ice extent~~ is calculated as the sum of area of all grid cells with ice concentration greater than 15%. Besides the total Arctic sea ice extent, we also calculate the ice extent for the following subregions: 1) Beaufort and Chukchi Seas (~~120W~~120°W-180, ~~60N-80N~~60°N-80°N), 2) East Siberian and Laptev Seas (~~90E~~90°E-180, ~~60N-80N),~~60°N-80°N), and 3) Barents, Kara, and Greenland Seas (~~30W-90E, 60N-80N), 4) Canadian Archipelago and Baffin Bay (30W-120W, 60N-80N).~~30°W-90°E, 60°N-80°N). To further assess the predictive skill of ~~our~~ Arctic sea ice predictions, ~~here~~ we ~~also~~ show the climatology prediction (CLIM, the period of 1998-

2017) and the damped anomaly persistence prediction (DAMP). Following Van den Dool (2006), the DAMP is generated from the initial sea ice extent anomaly (relative to the 1998-2017 climatology) scaled by the autocorrelation and the ratio of standard deviation between different lead times and initial times (see the DAMP equation in Y20).

In order to understand physical contributors that drive the evolving Arctic sea ice state, the mass budget of Arctic sea ice for all experiments is analyzed in this study as defined in Notz et al. (2016, Append. E), including 1) sea ice growth in supercooled open water (frazil ice formation), 2) basal growth, 3) snow-to-ice conversion, 4) top melt, 5) basal melt, 6) lateral melt, and 7) dynamics process.

3.2. Impacts of the RAP physics in the WRF model

To examine the performance of the upgrades of physical parameterization in component models in CAPS one step at a time compared to its predecessor in Y20, we define the Y21_CTRL experiment that uses the RAP physics in the WRF model (see Table 2 for differences between Y21_CTRL and Y20_MOD). Recently, the Rapid Refresh (RAP) model, a high-frequency weather prediction/assimilation modeling system operational at the National Centers for Environmental Prediction (NCEP), has made some improvements in the WRF model physics (Benjamin et al., 2016), including improved Grell-Freitas convection scheme (GF) and Mellor-Yamada-Nakanishi-Niino planetary boundary layer scheme (MYNN). For the GF scheme, the major improvements relative to the original scheme (Grell and Freitas, 2014) include: 1) a beta probability density function used as the normalized mass flux profile for representing height-dependent entrainment/detrainment rates within statistical-averaged deep convective plumes, which is given as:

$$Z_{u,d}(r_k) = c r_k^{\alpha} - (1 - r_k)^{\beta} - 1$$

where $Z_{u,d}$ is the mass flux profiles for updrafts and downdrafts, c is a normalization constant, r_k is the location of the mass flux maximum, α and β determine the skewness of the beta probability density function, and 2) the ECMWF approach used for momentum transport due to convection (Biswas et al. 2020; Freitas et al. 2018; 2021). For the MYNN scheme, the RAP model improves the mixing-length formulation, which is designed as:

$$\frac{1}{l_m} = \frac{1}{l_s} + \frac{1}{l_t} + \frac{1}{l_b}$$

where l_m is the mixing length, l_s is the surface length, l_t is the turbulent length, and l_b is the buoyancy length. Compared to the original scheme, the RAP model changed coefficients in the formulation of l_s, l_t, and l_b for reducing the near-surface turbulent mixing, and the diffusivity of the scheme. The RAP model also removes numerical deficiencies to better represent subgrid-scale cloudiness (Benjamin et al. 2016, see Append. B) compared to the original scheme (Nakanishi and Nino, 2009). In addition, some minor issues in the Noah land surface model (Chen and Dudhia, 2001) have been fixed, including discontinuous behavior for soil ice melting, negative moisture fluxes over glacial, and associated with snow melting.

Apparently, the above RAP physics can have influence on the behavior of simulated atmospheric thermodynamics (i.e., radiation, temperature). Figure 1 and 2 show the spatial distribution of the ERA5 surface downward solar and thermal radiation (SWDN and LWDN), the prediction errors (ensemble mean minuses ERA5) of Y20_MOD, and the difference between Y21_CTRL and Y20_MOD. For July, Y20_MOD (Fig. 1d) results in less SWDN over most of ocean basins as well as Alaska and northeast US, western Siberia, and eastern Europe, but more SWDN over southern and eastern Siberia compared with ERA5. For August and September (Fig. 1e-f), the spatial distribution is generally similar to that of July, except that eastern Siberia (less SWDN) and northern Canada (more SWDN) in August. It appears that the magnitude of the prediction errors tends to decrease over the areas with large prediction errors as the prediction time increases (i.e., July vs. September). Compared with Y20_MOD, the RAP physics in Y21_CTRL result in large areas with smaller prediction errors in July (e.g., the positive difference between Y21_CTRL and Y20_MOD reduces the negative prediction errors in Y20_MOD), except the north Pacific (especially the Sea of Okhotsk) and north Canada (Fig. 1g). For August and September (Fig. 1h, i), encouragingly, there are more areas with smaller prediction errors.

In contrast to SWDN, the prediction errors of LWDN in Y20_MOD has much smaller magnitude (up to 100 W/m^2 in SWDN vs. 50 W/m^2 in LWDN) for the entire prediction period (Fig. 2d-f). For July, Y20_MOD (Fig. 2d) simulates less LDWN over most of the model domain compared with ERA5, except the Atlantic sector and north Greenland. For August, the areas with negative prediction errors expand and the magnitude of prediction errors increases (particularly in southeastern Siberia and northeast US) compared to that of July (Fig. 2e). For September (Fig. 2f), the spatial distribution of LWDN is mostly similar to that of July, except that north Canada and Canadian Archipelago show positive prediction errors. The Y21_CTRL experiment with the RAP physics tends to reduce the prediction errors in Y20_MOD, especially over eastern Siberia and the Atlantic sector in July to September (Fig. 2g-i).

Figure 3 shows the spatial distribution of the ERA5 2m air temperature, the prediction errors of Y20_MOD, and the difference between Y21_CTRL and Y20_MOD. For Y20_MOD, the predicted air temperature in July has small cold prediction errors over all ocean basins, small-to-moderate cold prediction errors (~3-5 degrees) over Canada and Siberia, and moderate-to-large cold prediction errors (~6-9 degrees) over eastern Europe (Fig. 3d). ~~Compared to the Y20_MOD experiment, the Y21_CTRL experiment has ~0.5 million km^2 more ice extent at the initial, but the ice in Y21_CTRL melts~~In August (Fig. 3e), the cold prediction errors over most of the model domain are increased, in particular, very large cold prediction error (over 10 degrees) is located over east Siberia. In September, these cold prediction errors are decreased relatively, and some warm prediction errors are found in north of Greenland (Fig. 3f). With the adaptation of the RAP physics in the WRF model, Y21_CTRL, in general, produces a warmer state in most of the model domain compared to that of Y20_MOD during the entire prediction period. For July (Fig. 3g), the predicted air temperature is slightly warmer over the Arctic Ocean, the Pacific, and Atlantic sectors, moderately warmer (~1-2 degrees) over central and eastern Siberia and Canadian Archipelago, but the slightly colder over northern Canada than that of Y20_MOD. For August and September (Fig. 3h), most of the model domain is warmer in Y21_CTRL than that of Y20_MOD, in particular excessive cold prediction errors shown in Y20_MOD over Siberia are reduced notably (~2.5-4 degrees). We notice that the RAP physics does not have significant impacts on atmospheric circulation, given that Y21_CTRL and Y20_MOD have very similar wind pattern (not shown).

Figure 4 shows the temporal evolution of the ensemble mean of the predicted Arctic sea ice extent along with the NSIDC observations. In terms of the total ice extent, compared to the Y20_MOD experiment (blue line), the Y21_CTRL experiment (yellow line) produces ~0.5 million km^2 more ice extent at the initial. Note that the difference in the initial ice extent is related to that sea ice fields in Y20_MOD and Y21_CTRL (as well as other experiments listed in Table 2) are initialized based on one-month free runs (section 2), which use different physical configurations listed in Table 2. These one-month free runs do not have the same evolution in sea ice fields and result in different initial ice fields after data assimilation. The ice extent in Y21_CTRL decreases faster than Y20_MOD during the first 2-week integration. After that, they track each other closely, and predict nearly the same minimum ice extent (~4.3 million km^2). Like Y20_MOD, Y21_CTRL still has a delayed ice recovery in late September compared to the observation. Compared with the CLIM/DAMP predictions (black dashed and dotted lines), both Y20_MOD and Y21_CTRL have smaller ~~biases~~prediction errors in August, but comparable prediction errors after early ~~August. At the~~ September.

The difference in sea ice extent becomes larger at regional ~~scale,~~scales, in the East Siberian-Laptev Seas, Y20_CTRL shows faster ice decline after mid-July than that of Y21_MOD, whereas in the Beaufort-Chukchi Seas, Y21_CTRL predicts slower ice retreat after late July than that of Y20_MOD~~, whereas~~ (Fig. 4a, 4b). They are consistent with that Y21_CTRL predicts warmer (relatively colder) temperature than that of Y20_MOD in the East Siberian-Laptev (Beaufort-Chukchi) Seas~~, Y20_MOD shows slower ice decline after mid-July than that of Y21_CTRL (Fig. 3a, 3b).~~. Both Y20_MOD and Y21_CTRL agree well with the observations in the Barents-Kara-Greenland Seas (Fig. 4c). Compared with the observations, Y20_MOD performs relatively better in regional ice extents than that of Y21_CTRL. Figure 5 shows the spatial distribution of the NSIDC sea ice concentration and the difference between the predicted ice concentration and the observations for all grid cells that the predictions and the observations both have at least 15% ice concentration. The vertical and horizontal lining areas represent difference of the ice edge location. ~~3e). In the Baffin Bay-Canadian Archipelago, both Y20_MOD and Y21_CTRL have similar temporal evolution but show systematic underestimation of the observed areal extent (~ 0.3 million km^2, Fig.~~ Like the regional ice extent shown in Figure 4, Y21_CTRL predicts lower (higher) ice concentration along the East Siberian-Laptev (Beaufort-Chukchi) Seas (Fig. 5e$_1$-e$_3$). Y21_CTRL also predicts less ice in the central Arctic Ocean in August and September, which is consistent with warmer temperature in Y21_CTRL relative to Y20_MOD.~~3d). This underestimation is partly due to the difference in land/sea mask (particularly in the Canadian Archipelago) between our model grid and the NSIDC grid (not shown).~~

Figure ~~4~~6 shows the ~~spatial distribution~~evolution of ~~the NSIDC~~ sea ice ~~concentration and the difference between the predicted sea ice concentration and the observations for all grid cells that the predictions and the observations both have at least 15% ice concentration for the~~ mass budget terms of Y20_MOD and Y21_CTRL~~ experiments~~, averaged with cell-area weighting over the entire model domain. During the entire prediction period, most of the ice loss~~. The vertical and horizontal lining areas represent difference of the ice edge location. The distribution of the predicted ice concentration anomalies resembles~~ in ~~both~~ Y20_MOD and Y21_CTRL ~~experiments, except~~are caused by basal melting. The surface melting has relatively small contribution in the total ice loss and mainly occurs in July. However, compared with Y20_MOD (Fig. 6a), Y21_CTRL ~~predicts relatively higher ice concentration in~~ (Fig. 6b) shows much ~~of the Beaufort, Chukchi, and East Siberian Seas for the entire period (Fig. 4d-i).~~

larger magnitude for basal and surface melt. In a fully coupled predictive model, the changes of sea ice ~~is~~are determined by the fluxes from the atmosphere above and the ocean below. ~~The major difference between Y20_MOD and Y21_CTRL is the RAP physics improvements in the WRF model. The RAP physics improvements can have profound influence on the behavior of simulated atmospheric variables (i.e., radiation, temperature, humidity, precipitation,~~Associated with the increased downward radiation of the above RAP physics, Y21_CTRL absorbs more shortwave radiation (SWABS, Fig. 7a) and allows more penetrating solar radiation into the upper ocean below sea ice (SWTHRU, Fig. 7b) than that of Y20_MOD, especially in July. This explains why Y21_CTRL has larger magnitude of surface and basal melting terms. Although Y21_CTRL show larger magnitude in surface and basal melting than that of Y20_MOD, the ice extent in Y21_CTRL and Y20_MOD shown in Figure 4 show similar evolution. The effect of larger surface and ~~wind). Figure 5 shows the spatial distribution of the ERA5 2m air temperature (T2), the predicted anomalies (ensemble mean minuses ERA5) of Y20_MOD, and the difference between Y21_CTRL and Y20_MOD. For Y20_MOD, the predicted air temperature in July has small cold (warm) biases over all ocean basins (northern Greenland and eastern coastal Siberia), small-to-moderate cold biases (~3-5 degrees) over Canada and Siberia, and moderate-to-large cold biases (~6-9 degrees) over eastern Europe (Fig. 5d). In August (Fig. 5e), the cold biases over most of the model domain~~

~~are increased. In particular, very large cold bias (over 10 degrees) are located over east Siberia. In September, these cold biases are decreased, and warm biases are found in the north of Greenland and Canada (Fig. 5f). With the adaptation of the RAP physics in the updated WRF model, Y21_CTRL, in general, produces a warmer state~~basal melting in ~~most of the model domain compared to that of Y20_MOD during the entire prediction period. For July (Fig. 5g), the predicted air temperature is slightly warmer (< 1 degrees) over the Arctic Ocean, the Pacific, and Atlantic sectors, moderately warmer (~ 1-2 degrees) over the Siberia coast and Canadian Archipelago, but the slightly colder (<1 degrees) over northeastern Europe and northern Canada than that of Y20_MOD. For August (Fig. 5h), the Arctic Ocean and Atlantic sector (the Pacific sector and northern Canada) are relatively warmer (colder) than that of Y20_MOD. Excessive cold biases shown in Y20_MOD over Siberia are reduced notably (~2.5-4 degrees) in Y21_CTRL.~~Y21_CTRL is largely reflected in the ice thickness change. As ~~discussed above~~shown in Figure S3, Y21_CTRL has ~~faster~~thinner ice ~~melting~~thickness than that of Y20_MOD, in the East Siberian-Laptev Seas~~, which can be partly attributed to the changes in the predicted air temperature.~~ in July and in the much of central Arctic Ocean in August and September.

~~Figure 6 and Figure 7 shows the spatial distribution of the ERA5 downward solar and thermal radiation at the surface (SWDN and LWDN), the predicted anomalies (ensemble mean minuses ERA5) of Y20_MOD, and the difference between Y20_MOD and Y21_CTRL.~~

3.3. Impacts of the tracer advection in ROMS model

Currently~~For July, Y20_MOD (Fig. 6d) results in less SWDN over most of ocean basins,~~

~~southern Canada, western Siberia, and eastern Europe while more SWDN over southern and eastern Siberia, Canadian Archipelago, and northern Canada compared with ERA5. For August and September (Fig. 6e-f), the spatial distribution, in general, is similar to that of July, except that eastern Siberia, Canadian Archipelago and northern Canada have opposite sign. It also shows that the magnitude of biases decreases as the lead time decreases. With the RAP physics in the Y21_CTRL experiment, large areas have smaller biases compared with Y20_MOD in July (i.e., the positive difference between Y21_CTRL and Y20_MOD corresponds to the negative biases in Y20_MOD), except the north Pacific (especially the Sea of Okhotsk), southern Canada, and the central coastal Siberia (Fig. 6g). For August (Fig. 6h), there are more areas with smaller biases, but the north Pacific and southern Canada still have larger biases. In contrast to SWDN, the biases of LWDN shown in Y20_MOD has smaller magnitude (up to 100 W/m2 in SWDN vs. 50 W/m^2 in LWDN) for the entire prediction period (Fig. 7d-f). For July, Y20_MOD (Fig. 7d) shows less LDWN over most of the model domain compared with ERA5, except the Atlantic sector and north of Greenland. For August, areas with negative biases expand and the magnitude of biases increases (particularly in eastern and southern Siberia) compared with that of July (Fig. 7e). For September (Fig. 7f), the spatial distribution of LWDN is mostly similar to that of July, except that northern Canada and Canadian Archipelago show positive biases. The Y21_CTRL experiment with the RAP physics tends to reduce the negative biases shown in Y20_MOD, especially the negative biases over Siberia in August and September (Fig. 7g-i).~~

~~Associated with the change in surface fluxes, compared to Y20_MOD, Y21_CTRL shows~~

~~warmer SST along the ice edge in July, and the warm difference along the ice edge becomes larger (particularly near the east Siberian coast) in August and September. The other areas in Y21_CTRL are mostly with less than 0.2 degrees difference relative to Y20_MOD (Fig. 10g-i).~~

~~3.3. ROMS configuration~~

~~As described in section 2~~, the ROMS model that uses a generalized topography-following coordinate~~, but currently~~ has two vertical coordinate ~~transformations~~transformation options:

$$z(x,y,\sigma,t) = S(x,y,\sigma) + \zeta(x,y,t)\left[1 + \frac{S(x,y,\sigma)}{h(x,y)}\right] \quad (1)$$
$$S(x,y,\sigma) = h_c\sigma + [h(x,y) - h_c]C(\sigma)$$

or

$$z(x,y,\sigma,t) = \zeta(x,y,t) + [\zeta(x,y,t) + h(x,y)]S(x,y,\sigma)$$
$$S(x,y,\sigma) = \frac{h_c\sigma + h(x,y)C(\sigma)}{h_c + h(x,y)} \quad (2)$$

where $S(x,y,\sigma)$ is a nonlinear vertical transformation function, $\zeta(x,y,t)$ is the free-surface, $h(x,y)$ is the unperturbed water column thickness, $C(\sigma)$ is the non-dimensional, monotonic, vertical stretching function, and h_c controls the behavior of the vertical stretching. In Y20, we used the transformation ~~(~~1~~)~~ and the vertical stretching function introduced by Song and Haidvogel (1994~~) as the setup for seasonal Arctic sea-ice prediction.~~). However, the vertical transformation ~~(~~1~~)~~ has an inherent limitation for the value of h_c (expected to be the thermocline depth), which must be less than or equal to the minimum value in $h(x,y)$. As ~~the~~a result, h_c was chosen as 10 meters due to the limitation of the minimum value in $h(x,y)$ in Y20. This limitation is removed with the vertical transformation ~~(~~2~~) and h_c can be any positive value. Currently, the vertical transformation (2)~~ and the vertical stretching function introduced by Shchepetkin (2010), and h_c can be any positive value. ~~, the function in a research version of ROMS developed at University of California, Los Angeles, https://www.myroms.org/wiki/Vertical_S-coordinate) are employed. The~~ Here the Y21_VT experiment is ~~designed~~conducted to examine the ~~impacts~~impact of the vertical transformation in the ROMS model on seasonal Arctic sea ice simulation and prediction ~~by using~~, which uses the vertical transformation ~~(2),~~, the Shchepetkin stretching function, and 300 meters for h_c. As shown in Supplementary Figure S4-S5, compared to Y21_CTRL, Y21_VT is less sensitive to the bathymetry and its layers are more evenly-distributed in the upper 300 meters. With the changes of vertical layers of the upper ocean, the Y21_VT experiment has minor SST changes relative to Y21_CTRL. The simulated temporal evolution of total ice extent of Y21_VT (Fig. 4, red line) resembles to that of Y21_CTRL (Fig. 4, yellow line), although some differences are seen at the regional scale in the areas with shallow water (e.g., East Siberian, Laptev, Barents, and Kara Seas). The configuration of Y21_VT is used in the following experiments.

~~In pervious sensitivity experiments to determine the choice of ROMS physical parametrizations listed in Table 2, we noticed~~It has been recognized that the tracer advection and the vertical mixing schemes have important effects on ocean and sea ice simulation~~. Thus here~~ (e.g., Liang and Losch, 2018; Naughten et al., 2017). Here the Y21_RP experiment is designated to ~~further~~ explore the influence of ~~these~~ different advection schemes in the ~~updated CAPS, in which~~ROMS model. Specifically, the tracer advection scheme is changed from the Multidimensional positive definite advection transport algorithm (MPDATA; Smolarkiewicz, 2006) to the third-order upwind horizontal advection (U3H; Rasch, 1994; Shchepetkin, and

McWilliams, 2005) and the fourth-order centered vertical advection schemes (C4V; Shchepetkin, and McWilliams, 1998; 2005). The MPDATA scheme applied in Y20_MOD, Y21_CTRL, and Y21_VT is a non-oscillatory scheme but a sign preserving scheme (Smolarkiewicz, 2006) that means MPDATA is not suitable for tracer fields having both positive and negative values (i.e., temperature with degree Celsius in the ROMS model). The upwind third-order (U3H) scheme used in Y21_RP is an oscillatory scheme but it significantly reduces oscillations compared to other centered schemes (e.g., Hecht et al., 2000; Naughten et al., 2017) available in the ROMS model.

~~The temporal evolutions of the ensemble mean of the predicted Arctic total sea ice extent (as well as regional ice extent) for Y21_CTRL, Y21_VT, and Y21_RP are shown in~~ Figure 8~~. Y21_VT (green line) simulates slightly less areal extent (<0.1 million km^2) compared to that of Y21_CTRL throughout the prediction period. The Y21_RP~~ shows ~~highly similar temporal evolution of areal extent as Y21_CTRL until near the end of August. After that, the ice melting slows down and ice extent begins to recover earlier in Y21_RP (red line) compared to both Y21_CRTL and Y21_VT, which leads to much smaller biases in seasonal minimum ice extent relative to the observation. This result suggests the delayed ice recovery in late September shown in Y20, Y20_MOD and Y21_CTRL is partly due to the choice of ocean advection and vertical mixing schemes that change the behavior of oceanic state. Y21_RP also shows much better predictive skill after late August compared with the CLIM/DAMP predictions (black dashed and dotted lines). At the regional scale, changes in both the ocean vertical coordinate (Y21_VT) and the advection and vertical mixing scheme (Y21_RP) do not significantly affect~~

~~the evolution of areal extent in the Barents-Kara-Greenland Seas and the Baffin Bay-Canadian Archipelago compared to that of Y21_CTRL (Fig. 8c, d). However, Y21_VT agrees better with the observations in the Beaufort-Chukchi Seas and the East Siberian-Laptev Seas compared to that of Y21_CTRL and the ice extent of Y21_RP stops retreating after mid-September in the Beaufort-Chukchi Seas relative to that of Y21_CTRL (Fig. 8a, b).~~

~~Spatially, the choice of vertical transformation in Y21_VT does not significantly change the distribution of sea ice biases in Y21_CTRL (i.e., higher ice concentration in the Pacific sector, and lower ice concentration in the Atlantic sector, (Fig. 9a-c, Fig. 4g-i). The Y21_VT experiment has slightly lower ice concentration compared with that of Y21_CTRL, which corresponds to less areal extent of Y21_VT shown in Figure 8. By using U3H/C4V advection scheme, the Y21_RP experiment has positive anomalies for most ice-covered areas (Fig. 9d-f). For September, the Y21_RP experiment better predicts the ice edge location in the Atlantic sector of the Arctic Ocean (i.e., smaller areas with horizontal/vertical lining) compared to the experiments described above (Fig. 9f).~~

~~Figure 10 shows that~~the spatial distribution of the SST changes of Y21_VT and Y21_RP relative to Y21_CTRL (as well as ~~predicted anomalies of Y20_MOD~~the OI SST and the difference between Y21_CTRL and ~~Y21_MOD). By using different vertical transformation in the ROMS model, the Y21_VT experiment simulates slightly warmer SST in the north Pacific and Atlantic (~0.5 degree), and colder SST in the Bering Sea, Sea of Okhotsk, Barents-Kara, and Greenland Seas (~0.5-1.0 degree). We also note that SST under sea ice cover is warmer than that of Y21_CTRL, especially in the Beaufort-Chukchi Seas, which results in larger~~

~~temperature difference and thus heat fluxes at the ice-ocean interface, and then contributes to faster ice retreating in the Beaufort-Chukchi Seas (Fig. 10j-l, Fig. 8a). With~~ OISST). In general, Y21_CTRL shows cold prediction errors in the North Pacific (~2 degrees) and the Atlantic (~3 degrees) compared to that of OISST in July, and these cold prediction errors are enhanced as the prediction time increases (to 3-5 degrees, Fig. 8d-f). With the U3H/C4V tracer advection scheme in Y21_RP, cold ~~biases~~prediction errors shown in Y21_CTRL ~~(Fig. 10d-i)~~ are reduced significantly in the north Pacific and Atlantic, but SST under sea ice ~~cover~~in much of the Arctic Ocean is slightly colder than that of Y21_CTRL (Fig. ~~10m-o~~8j-l).

~~**3.4. CICE configuration and ice thickness assimilation**~~

Y21_RP (Fig. 4, green line) shows comparable temporal evolution of the ice extent as Y21_CTRL (as well as Y21_VT) until near the end of July. After that, the ice melting slows down (closer to the observation) and the ice extent begins to recover earlier (after the first week of September) in Y21_RP compared to Y21_CRTL. This leads to much smaller prediction error in seasonal minimum ice extent relative to the observation. Y21_RP also shows better predictive skill after late August compared with the CLIM/DAMP predictions (black dashed and dotted lines). This suggests the delayed ice recovery in late September shown in Y20_MOD, Y21_CTRL and Y21_VT is in part due to the choice of ocean advection and vertical mixing schemes, which change the behavior of ocean state. At the regional scale, the slower ice decline after July and earlier recovery of the ice extent in September mainly occur in the Beaufort-Chukchi and Barents-Kara-Greenland Seas compared to that of Y21_CTRL (Fig. 4a, c). By using U3H/C4V scheme, the Y21_RP experiment simulates higher sea ice concentration than that of Y21_VT (Fig. 5f_1-f_3). For September, the Y21_RP experiment better predicts the ice edge location in the Atlantic sector of the Arctic (i.e., smaller areas with horizontal/vertical lining) compared to the experiments described above (not shown).

Figure 9 shows the evolution of sea ice mass budget terms of Y21_VT and Y21_RP. Relative to Y21_VT, Y21_RP (with U3H/C4V scheme) results in increased frazil ice formation in July, which is partly compensated by increased surface melting. Y21_RP also leads to increased basal growth in mid- and late September (Fig. 9a, b).

Figure 10 shows the difference in the vertical profile of ocean temperature and salinity in the upper 150 m averaged for the central Arctic Ocean between Y21_RP and Y21_VT. The ocean temperature in the surface layer of Y21_RP is slightly colder during the prediction period compared to that of Y21_VT (Fig. 10a), especially in August and September. Moreover, the water in the surface layer (0-20 m) of Y21_RP is fresher than that of Y21_VT (Fig. 10b). They reduce the freezing temperature and favor frazil ice formation. In the CAPS, the frazil ice formation is determined by the freezing potential, which is the vertical integral of the difference between temperature in upper ocean layer and the freezing temperature in the upper 5 m-layer. The supercooled water is adjusted based on the freezing potential to form new ice and rejects brine into the ocean that leads to saltier water between 20-50 m in Figure 10. It should be noted that the increased frazil ice formation in July in Y21_RP might be also partly due to the oscillatory behavior of U3H scheme, which makes the temperature fall below the freezing point and then instantaneously forms new ice (as well as temperature/salinity adjustments).

3.4. Impacts of sea ice thermodynamics in the CICE model

In Y20, we used ~~the~~sea ice thermodynamics introduced by Bitz and Lipscomb (1999; hereafter BL99~~),~~) as the setup of CAPS, which assumes a fixed vertical salinity profile based on observations~~, as the setup for seasonal Arctic sea ice prediction. Since the release of~~. The new CICE ~~version 5, it~~ model includes ~~the~~a MUSHY-layer ice thermodynamics introduced by Turner et al. (2013), which simulates vertically ~~resolved~~ and time-varying prognostic salinity and ~~its~~ associated ~~impact~~effects on ~~other thermodynamics~~thermodynamic properties of sea ice. In the Y21_MUSHY experiment, we change the ice thermodynamics from BL99 to MUSHY (Table ~~3~~2) to examine whether improved ice thermodynamics has noticeable influence on Arctic sea ice simulation and prediction at seasonal timescale. ~~Additionally, in Y20 and~~Compared to Y21_RP, Y21_MUSHY (Fig. 4, pink line) produces very similar evolution of the total ice extent. However, it simulates relatively larger ice extent near the end of September, which is also reflected by the basin-wide increased ice cover shown in Figure $5h_3$. At the regional scale, compared to Y21_RP, Y21_MUSHY predicts less ice in August in the Beaufort-Chukchi. The opposite is the case for the East Siberian-Laptev Seas (Fig. 4a, b).

Figure 11 shows the difference of the ensemble mean of the predicted ice thickness between Y21_MUSHY and Y21_RP. Compared with Y21_RP, Y21_MUSHY simulates thicker ice (from ~0.2m in July to over 0.4m in September) extending from the Canadian Arctic, through the central Arctic Ocean, to the Laptev Sea (Fig. 11a-c). This seems to be consistent with previous studies, which show that the Mushy-layer thermodynamics simulates thicker ice than BL99 thermodynamics in both standalone CICE (Turner and Hunke, 2015) and the fully-coupled (Bailey et al., 2020), but Y21_MUSHY shows thinner ice (~0.2m) in an arc extending from north of Alaska to north of eastern Siberia compared to Bailey et al. (2020). Note that Y21_MUSHY focuses the effects of Mushy-thermodynamics on seasonal timescale while the results in Bailey et al. (2020) are based on 50-year simulations.

Compared to Y21_RP, the mass budget of Y21_MUSHY (Fig. S6) shows that both surface melting and frazil ice formation terms are increased. This compensation between surface melting and frazil ice formation from the Mushy-layer thermodynamics in the CAPS leads to relatively unchanged total ice extent between Y21_MUSHY and Y21_RP (Fig. 4 green and pink lines).

4. Prediction skill of CAPS at longer timescale

The design of Arctic sea ice prediction experiments described above follow the protocol of the Sea Ice Prediction Network (SPIN), in which the outlook start from June 1st, July 1st, and August 1st to predict seasonal minimum of the ice extent in September. It is not clear that how predictive skills of dynamical models participating in SIPN may change for longer period. Here we conduct two more experiments to investigate the predictive capability of CAPS beyond the SPIN prediction period. For the prediction experiments discussed above, we use a simple approach to merge CryoSat-2 and SMOS ice thickness by replacing ice thickness less than 1m in CryoSat-2 data with SMOS data for ice thickness assimilation. Ricker et al. (2017) presented a new ice thickness product (CS2SMOS) based on the optimal interpolation to statistically merge CrySat-2 and SMOS data. ~~The Y21_SIT experiment (Table 3) is designed to~~

~~investigate~~Here we utilize the ~~impacts~~configuration of ~~assimilating different approaches to merge CyroSat-2 and SMOS data on sea ice prediction .~~

~~Figure 11 shows the temporal evolutions of the ensemble mean of the predicted Arctic total sea ice extent (as well as regional ice extent) for the~~ Y21_RP~~, Y21_MUSHY, and~~ but use CS2SMOS SIT for the assimilation (Y21_SIT~~ experiments. All three experiments predict~~; Table 2). The predicted total ice extent is almost identical ~~total ice extents during the first 2-week integration. After that, Y21_MUSHY (red solid line) produces a slightly more ice extent (~0.2 million km~~^{2}~~) than that of Y21_RP (blue solid line) for the rest of integration, which mainly due to an increase of sea ice in the East Siberian-Laptev Seas (Fig. 11b). The timing of minimum ice extent occurs early in Y21_MUSHY relative to Y21_RP, resulting in early recovery. In contrast to Y21_RP, Y21_SIT (green solid line) simulates~~to Y21_RP in July but slightly larger ~~ice~~total extent after ~~the first week of August. At the regional scale, compared with Y21_RP, Y21_SIT predicts more ice before the mid-August and less ice after that in the Beaufort-Chukchi Seas (Fig. 11a) and larger ice extent throughout the entire prediction period in the Barents-Kara-Greenland Seas (Fig. 11c). For the spatial distribution of ice concentration anomalies, Y21_MUSHY and Y21_SIT show similar distribution as Y21_RP with slightly higher ice concentration at gridpoint scale (~~July than that of Y21_RP (not shown).

~~Figure 12 show the ensemble mean of predicted sea ice thickness of the Y21_RP, Y21_MUSHY, and Y21_SIT experiments and the ice thickness changes of Y21_MUSHY and Y21_SIT relative to Y21_RP. All three experiments produce similar ice thickness distribution, that~~ The configuration of Y21_SIT is ~~the thickest ice locates near the Canadian Archipelago~~

~~and the Lincoln Sea, as well as the thickness gradient directs toward the Siberia coast (Fig. 12a-f). Compared with Y21_RP, Y21_MUSHY simulates thicker ice (from ~0.14m in July to over 0.2m in September) in the Canadian Arctic and the central Arctic Ocean, thinner ice (over 0.2m) in the Kara Sea in September, and negligible thickness difference in other areas (Fig. 12g_1-i_1). This is consistent with previous studies showing that the Mushy layer thermodynamics simulates thicker ice than BL99 thermodynamics in both standalone CICE (Turner and Hunke, 2015) and the fully coupled context~~ (used in the following experiments. Taking advantage of the ~~Bailey et al.,~~ ~~2020). Compared with Y21_RP, Y21_SIT predicts thicker ice most of the ice edge zone and thinner ice in the central Arctic Ocean in July and August. In September, Y21_SIT simulates much thinner ice (over 0.2m) in the Beaufort, Chukchi, East Siberian Seas, and the central Arctic Ocean along with thicker ice in the Barents, Kara, and Laptev Seas (Fig. 12g_2-i_2). The evolution of predicted ice thickness in Y21_SIT corresponds to that of regional ice extent shown in Figure 11. This result suggests that assimilating the new ice thickness product (CS2SMOS) have significant influences on the predicted ice thickness at the regional scale.~~

~~**4. Discussions**~~

~~Arctic sea ice prediction experiments conducted in this study follow the protocol of Sea Ice Prediction Network (SPIN), in which the outlook start from June 1^{st}, July 1^{st}, and August 1^{st} to predict seasonal minimum of ice extent in September. Due to the socioeconomic impacts of sea ice recovery during the freeze-up period (e.g., trans-Arctic shipping, coastal activities), it is also essential to investigate the predictive capability of CAPS beyond the SPIN prediction~~

~~period. Combining the~~ entire prediction period provided by CFS forecasts ~~and the Y21_SIT experiment,~~(7 months), the Y21_EXT-7 experiment is designed to extend the prediction period to the end of January next year (Table ~~3~~2). Figure ~~13~~12 shows the temporal ~~evolutions~~evolution of the ensemble mean of the predicted total Arctic ~~total~~ sea ice extent (as well as regional ice extent) for ~~the~~ Y21_EXT-7~~ experiment. As shown in Figure 13, the predicted~~. The total ice extent exhibits reasonable evolution in terms of seasonal minimum and timing of recovery compared with the observations until late November. Y21_EXT-7 also performs better than that of the CLIM/DAMP predictions (black dashed and dotted lines) until mid-to-late November. After that, Y21_EXT-7 overestimates the total ice extent ~~compared with~~relative to the observations, and ~~this~~such overestimation is largely contributed by more extensive sea ice in the Barents-Kara-Greenland Seas (Fig. ~~13c). The overestimated ice cover in the Barents-Kara-Greenland Seas may be the results of biases from the CFS data propagated into the model domain through lateral boundary conditions and accumulated effects of biases in model components.~~12c), which is a result of a sharp increase in the basal growth term after mid-to-late November (not shown).

A growing number of studies have shown evidences of Arctic sea ice spring predictability barrier~~, which is defined as a springtime date~~. It means that predictions initialized prior to ~~this date~~spring (before May) have much lower predictive skill than predictions initialized after/on that date (e.g., Bonan et al., 2019; Bushuk et al., 2017; 2018; Day et al., 2014). To investigate the predictive capability of CAPS initialized prior to the summer melting season, the Y21_MAR-7 experiment is initialized on March 1st, 2018 and predicts sea ice evolution until the end of September (Table ~~3~~2). Figure ~~14~~13 shows the temporal ~~evolutions~~evolution of the ensemble mean of the predicted total Arctic ~~total~~ sea ice extent (as well as regional ice extent) for the Y21_MAR-7 experiment. The evolution of predicted total sea ice extent shows faster ice melting rate than the observations after mid-May, but slower ice retreating after mid-July~~,~~ ~~and~~. As a result, the predicted minimum of ice extent has an overestimation (~1.2 million km^2) compared to the observed minimum. In contrast to Y21_MAR-7, the DAMP prediction (black dotted line) agrees better with the observations throughout the 7-month prediction period. At the regional scale, Y21_MAR-7 shows abrupt ice decline after May in the Beaufort-Chukchi Seas (Fig. ~~14a~~13a), and this decline is mainly contributed by ice ~~melting~~retreating along the Alaskan coast (not shown). Sea ice in the East Siberian-Laptev Seas exhibits slow melting after July (Fig. ~~14b~~13b), and ice cover ~~areas~~ still connect to the Siberian coast, which is different from the observations (not shown). For the Barents-Kara-Greenland Seas (Baffin Bay-Canadian Archipelago), there are systematic overestimations (underestimations) throughout the entire prediction period (Fig. ~~14c~~13c-d). Bushuk et al. (2020) suggested that Arctic sea ice predictability prior to the barrier date is mainly limited by synoptic events, which are only predictable for few weeks, whereas the predictability after the barrier date is enhanced by ice-albedo feedback with the onset of ice melting.

5. Conclusions and Discussions

This paper presents and evaluates the updated Coupled Arctic Prediction System (CAPS) designated for Arctic sea ice ~~and climate prediction. The CAPS consists of the WRF, ROMS,~~

~~and CICE models under the framework of the COAWST system, as well as data assimilation system based on the localized error subspace transform ensemble Kalman filter to assimilate satellite-observed sea ice observations~~prediction through a case study for the year of 2018. A set of Pan-Arctic prediction experiments with improved/changed physical parameterizations as well as different configurations starting from July 1st to the end of September are performed for ~~the year of~~ 2018 to assess their impacts of the updated CAPS on the predictive skill of Arctic sea ice at seasonal timescale. Specifically, we focus on the Rapid Refresh (RAP) physics in the WRF model, the oceanic tracer advection scheme in the ROMS model, sea ice thermodynamics in the CICE model, and investigate physical process linking them to Arctic sea ice simulation and prediction.

The results ~~of prediction experiments~~ show that the updated CAPS with improved physical parameterizations can better predict the evolution of the total ice extent compared with its predecessor described in Yang et al. ~~(2020), though the predictions exhibit biases in regional ice extent. We demonstrate that the~~(2020), though the predictions exhibit some prediction errors in regional ice extent. The key improvements of WRF, including cumulus, boundary layer, and land surface schemes, result in improved simulations in downward radiative fluxes and near surface air temperature. These improvements mainly influence the predicted ice thickness instead of total ice extent. The difference in the predicted ice thickness can have potential impacts on the icebreakers planning their routes across the ice-covered regions. The major changes of ROMS, including tracer advection and vertical mixing schemes, reduces the prediction error in sea surface temperature and changes ocean temperature and salinity structure in the surface layer, leading to improved evolution of the predicted total ice extent (particularly correcting the late ice recovery issue in the previous CAPS). The change of CICE, including improved ice thermodynamics, have noticeable influences on the predicted ice thickness.

We demonstrate that CAPS can remain skillful beyond the designated period of Sea Ice Prediction Network (SIPN), which has potential values for stakeholders making decisions regarding the socioeconomical activities. ~~Along with the improved~~Although CAPS shows extended predictive skill to the freeze-up period, the prediction produces extensive ice through the basal growth near the end of ~~total~~ prediction. The excessive basal growth may be partly due to that the bias of the CFS data propagates into the model domain through lateral boundary conditions and its accumulated effect influences Arctic sea ice ~~extent, the~~ simulation during the freeze-up period.

Keen et al. (2021) analyzed the Arctic mass budget of 15 models participated in the Coupled Model Intercomparison Project Phase 6 (CMIP6). We notice that, first, the top melting and the basal melting terms in CMIP6 models have comparable contributions in July while the top melting term only has ~50% contribution relative to the basal melting term in the CAPS. The updated CAPS ~~also has reduced biases in~~with the ~~predicted near~~RAP physics improves the performance of shortwave/longwave radiation at the surface ~~air temperature, downward radiations~~(Fig. 1 and Fig. 2). The net flux at the surface, ~~and sea surface~~ however, may still be underestimated in the CAPS. Besides, the surface property of sea ice (i.e., the amount of melt ponds, bare ice, and snow) is a factor that influences surface albedo and thus the absorbed shortwave radiation (e.g., Nicolaus et al., 2012; Nicolaus and Katlein, 2013). The prediction experiments starting at July 1st in this study do not consider the initialization of melt ponds (i.e., zero melt pond coverage at the initial). However, melt ponds start to develop in early May based on the satellite observations (e.g., Liu et al., 2015, Fig. 1). The initialization of melt pond based on the observations (e.g., Ding et al., 2020) in the CAPS is a direction to improve the representation of the ice surface properties. Second, the mass budget analysis by both Keen et al. (2021) and this study show that the contribution of lateral melting term is relatively small, which might be due to that CMIP6 models and the CAPS assume constant floe-size (i.e., 300 meters in CICE), which is a critical value to determine the strength of lateral melting (e.g., Horvat et al., 2016; Steele, 1992). Recently, several studies have proposed floe size distribution models (e.g., Bateson et al., 2020; Bennetts et al., 2017; Boutin et al., 2020; Horvat and Tziperman, 2015; Roach et al., 2018, 2019; Zhang et al., 2015, 2016). Incorporating floe size distribution model in the CAPS and understanding its impacts on seasonal Arctic sea ice prediction will be a future direction of developing CAPS. Lastly, the prediction experiments with the upwind advection scheme (i.e., Y21_RP, Y21_EXT-7) shows spurious large frazil ice formation, particularity in July, which is different from the analysis shown in Keen et al. (2021). An approach for reducing spurious frazil ice formation is proposed by Naughten et al. (2017) that they implemented upwind limiter (Leonard and Mokhtari, 1990) to the U3H scheme to further reduce the oscillations. Naughten et al. (2018) also suggested that the oscillatory behaviors can be smoothed out by applying the Akima fourth-order tracer advection scheme combined with Laplacian horizontal diffusion at a level strong enough. Beside of the oscillatory behaviors of advection scheme, the ice-ocean heat flux can also play a role in the spurious frazil ice formation. As discussed in section 3.3, the freezing/melting potential not only determines the amount of newly-formed ice, but also limits the amount of energy that can be extracted from the ocean surface layer to melt sea ice. This implies that the ocean surface layer will be close to the freezing temperature if the ice-ocean heat fluxes reach the limit imposed by the melting potential. Shi et al. (2021) discussed the impacts of different ice-ocean heat flux parametrizations on sea ice simulations. Their results suggest that Arctic sea ice will be thicker and ocean temperature ~~in Arctic domain compared to its predecessor.~~ will warmer beneath high-concentration ice with a complex approach proposed by Schmidt et al. (2004) that limits melt rates (heat fluxes) of sea ice through considering a fresh water layer underlying sea ice. The warmer ocean temperature under sea ice with a more complex approach in ice-ocean heat flux may be the solution to reduce the occurrence of local temperature falling below freezing temperature with oscillatory advection schemes.

Based on the prediction experiments discussed in ~~the~~this paper, the configuration ~~of the~~ with the RAP physics, the U3H/C4V ocean advection, BL99 ice thermodynamics, and CS2SMOS ice thickness assimilation (Table 2, Y21_SIT~~ experiment~~) is assigned as the finalized CAPS version 1.0. Improving the representation of physical processes in the CAPS version 1.0 for further reducing the model bias will remain the main focus for the development of CAPS~~ version 1.0.~~

. Since the CAPS ~~version 1.0~~ is a regional modeling system, it relies on ~~GCM~~the forecasts form global climate models as initial and lateral boundary conditions. That is, biases existed in

GCM simulations (here the CFS forecast) can be propagated into and affect the entire area-limited domain (e.g., Bruyère et al., 2014; Rocheta et al., 2020; Wu et al., 2005). This issue can be a potential source that influences the predictive capability of CAPS ~~version 1.0~~ for longer timescales. Studies have applied bias correction techniques with different complexities for improving the performance of regional modeling system (e.g., Bruyère et al., 2014; Colette et al., 2012; Rocheta et al., 2017, 2020). Further investigation is needed to address biases inherited from GCM predictions through lateral boundaries for improving the predictive capability of CAPS ~~version 1.0~~.

Code and data availability: The COAWST and CICE models are open source and can be downloaded from their developers at https://github.com/jcwarner-usgs/COAWST and https://github.com/CICE-Consortium/CICE, respectively. PDAF can be obtained from https://pdaf.awi.de/trac/wiki. CAPS v1.0 described in this paper is permanently archived at https://doi.org/10.5281/zenodo.5034971. The prediction data analyzed in this paper can be accessed from https://doi.org/10.5281/zenodo.4911415.

Author contributions: CYY and JL designed the model experiments, developed the updated CAPS model, and wrote the manuscript, CYY conducted the prediction experiments and analyzed the results. DC provided constructive feedback on the manuscript.

Competing interests: The authors declare that they have no conflict of interest.

Acknowledgements: This research is supported by the National Natural Science Foundation of China (42006188), the National Key R&D Program of China (2018YFA0605901), and the Innovation Group Project of Southern Marine Science and Engineering Guangdong Laboratory (Zhuhai) (311021008). The authors also acknowledge the National Centers for Environmental Prediction for providing CFS seasonal forecasts, the University of Hamburg for distributing the SMOS sea ice thickness data, the Alfred-Wegener-Institut, Helmholtz Zentrum für Polar- und Meeresforschung for providing the CryoSat-2 sea ice thickness data and CS2SMOS data, the Polar Science Center for distributing the PIOMAS ice thickness data, the National Snow and Ice Data Center for providing the SSMIS sea ice concentration data, the European Centre for Medium-Range Weather Forecasts for distributing the ERA5 reanalysis, and the National Oceanic and Atmospheric Administration for providing the OI sea surface temperature.

6. References

Aagaard, K.: A synthesis of the Arctic Ocean circulation. Rapp. P.-V. Reun.- Cons. Int. Explor. Mer, 188, 11–22, 1989.

Bailey, D. A., Holland, M. M., DuVivier, A. K., Hunke, E. C., and Turner, A. K.: Impact of a new sea ice thermodynamic formulation in the CESM2 sea ice component. Journal of Advances in Modeling Earth Systems, 12, e2020MS002154. https://doi.org/10.1029/2020MS002154, 2020.

Bateson, A. W., Feltham, D. L., Schröder, D., Hosekova, L., Ridley, J. K., and Aksenov, Y.: Impact of sea ice floe size distribution on seasonal fragmentation and melt of Arctic sea ice, The Cryosphere, 14, 403–428, https://doi.org/10.5194/tc-14-403-2020, 2020.

Bitz, C. M. and Lipscomb, W. H.: An energy-conserving thermodynamic sea ice model for climate study. J. Geophys. Res.-Oceans, 104, 15669–15677, 1999.

Benjamin, S. G., Weygandt, S. S., Brown, J. M., Hu, M., Alexander, C. R., Smirnova, T. G. and Manikin, G. S.: A North American hourly assimilation and model forecast cycle: the Rapid Refresh. Monthly Weather Review, 144,1669–1694. https://doi.org/10.1175/MWR-D-15-0242.1, 2016.

Bennetts, L. G., O'Farrell, S., and Uotila, P.: Brief communication: Impacts of ocean-wave-induced breakup of Antarctic sea ice via thermodynamics in a stand-alone version of the CICE sea-ice model, The Cryosphere, 11, 1035–1040, https://doi.org/10.5194/tc-11-1035-2017, 2017.

Biswas, M. K., Zhang, J. A., Grell, E., Kalina, E., Newman, K., Bernardet, L., Carson, L., Frimel, J., and Grell, G.: Evaluation of the Grell–Freitas Convective Scheme in the Hurricane Weather Research and Forecasting (HWRF) Model, Weather and Forecasting, 35(3), 1017-1033, 2020.

Blanchard-Wrigglesworth, E., Bitz, C., and Holland, M.: Influence of initial conditions and climate forcing on predicting Arctic sea ice. Geophysical Research Letters, 38, L18503. https://doi.org/10.1029/2011GL048807, 2011.

Blanchard-Wrigglesworth, E., and Bushuk, M.: Robustness of Arctic sea-ice predictability in GCMs. Climate Dynamics, 52, 5555–5566, 2018.

Blanchard-Wrigglesworth, E., Cullather, R., Wang, W., Zhang, J., and Bitz, C. M.: Model forecast skill and sensitivity to initial conditions in the seasonal sea ice outlook. Geophysical Research Letters, 42, 8042–8048. https://doi.org/10.1002/2015GL065860, 2015.

Bonan, D., Bushuk, M., and Winton, M.: A spring barrier for regional predictions of summer Arctic sea ice. Geophysical Research Letter, 46, 5937–5947. https://doi.org/10.1029/2019GL082947, 2019.

Boutin, G., Lique, C., Ardhuin, F., Rousset, C., Talandier, C., Accensi, M., and Girard-Ardhuin, F.: Towards a coupled model to investigate wave–sea ice interactions in the Arctic marginal ice zone, The Cryosphere, 14, 709–735, https://doi.org/10.5194/tc-14-709-2020, 2020.

Briegleb, B. P. and Light, B.: A Delta-Eddington multiple scattering parameterization for solar radiation in the sea ice component of the Community Climate System Model. NCAR Tech. Note NCAR/TN-472+STR, National Center for Atmospheric Research, 2007.

Bruyère, C. L., Done, J. M., Holland, G. J., and Fredrick, S.: Bias corrections of global models for regional climate simulations of high-impact weather. Clim Dyn 43, 1847–1856 (2014). https://doi.org/10.1007/s00382-013-2011-6, 2014.

Bushuk, M., Msadek, R., Winton, M., Vecchi, G., Gudgel, R., Rosati, A., and Yang, X.: Skillful regional prediction of Arctic sea ice on seasonal timescales. Geophysical Research Letter, 44, 4953–4964. https://doi.org/10.1002/2017GL073155, 2017.

Bushuk, M., Msadek, R., Winton, M., Vecchi, G., Yang, X., Rosati, A., and Gudgel, R.: Regional Arctic sea-ice prediction: Potential versus operational seasonal forecast skill. Climate Dynamics, 52, 2721–2743, 2018.

Bushuk, M., Winton, M., Bonan, D. B., Blanchard-Wrigglesworth, E., and Delworth, T. L.: A mechanism for the Arctic sea ice spring predictability barrier. Geophysical Research Letters, 47, e2020GL088335. https://doi.org/10.1029/2020GL088335, 2020.

Carmack, E., Polyakov, I., Padman, L., Fer, I., Hunke, E., Hutchings, J., Jackson, J., Kelley, D., Kwok, R., Layton, C., Melling, H., Perovich, D., Persson, O., Ruddick, B., Timmermans, M.-L., Toole, J., Ross, T., Vavrus, S., and Winsor, P.: Toward Quantifying the Increasing Role of Oceanic Heat in Sea Ice Loss in the New Arctic. Bulletin of the American Meteorological Society 96, 12, 2079-2105, https://doi.org/10.1175/BAMS-D-13-00177.1, 2015.

Cavalieri, D. J., Parkinson, C. L., Gloersen, P., and Zwally, H. J.: updated yearly. Sea Ice Concentrations from Nimbus-7 SMMR and DMSP SSM/I-SSMIS Passive Microwave Data, Version 1. Boulder, Colorado USA. NASA National Snow and Ice Data Center Distributed Active Archive Center. https://doi.org/10.5067/8GQ8LZQVL0VL, 1996.

Chen, F. and Dudhia, J.: Coupling an advanced land surface–hydrology model with the Penn State–NCAR MM5 modeling system. Part I: Model implementation and sensitivity. Mon. Wea. Rev., 129, 569–585, 2001.

Chevallier, M., Salas y Mélia, D., Voldoire, A., Déqué, M., and Garric, G.: Seasonal forecasts of the pan-Arctic sea ice extent using a GCM-based seasonal prediction system. Journal of Climate, 26(16), 6092–6104, 2013.

Colette, A., Vautard, R., and Vrac, M.: Regional climate downscaling with prior statistical correction of the global climate forcing, Geophys. Res. Lett., 39, L13707, https://doi.org/10.1029/2012GL052258, 2012.

Day, J. J., Tietsche, S., Collins, M., Goessling, H. F., Guemas, V., Guillory, A., et al.: The Arctic predictability and prediction on seasonal-to-interannual timescales (apposite) data set version 1. Geoscientific Model Development, 9, 2255–2270, 2016.

Day, J., Tietsche, S., and Hawkins, E.: Pan-Arctic and regional sea ice predictability: Initialization month dependence. Journal of Climate, 27(12), 4371–4390, 2014.

Ding, Y., Cheng, X., Liu, J., Hui, F., Wang, Z., and Chen, S.: Retrieval of Melt Pond Fraction over Arctic Sea Ice during 2000–2019 Using an Ensemble-Based Deep Neural Network. Remote Sensing. 12(17):2746. https://doi.org/10.3390/rs12172746, 2020

DuVivier, A. K., Holland, M. M., Landrum, L., Singh, H. A., Bailey, D. A., and Maroon, E. A.: Impacts of sea ice mushy thermodynamics in the Antarctic on the coupled Earth system. Geophysical Research Letters, 48, e2021GL094287. https://doi.org/10.1029/2021GL094287, 2021.

Fer, I.: Near-inertial mixing in the central Arctic Ocean. J. Phys. Oceanogr., 44, 2031–2049, https://doi.org/10.1175/JPO-D-13-0133.1, 2014.

Fetterer, F., Knowles, K., Meier, W. N., Savoie, M., and Windnagel, A. K.: updated daily. Sea Ice Index, Version 3. Boulder, Colorado USA. NSIDC: National Snow and Ice Data Center. https://doi.org/10.7265/N5K072F8, 2017.

Freitas, S. R., Grell, G. A., Molod, A., Thompson, M. A., Putman, W. M., Santos e Silva, C. M. and Souza, E. P.: Assessing the Grell–Freitas convection parameterization in the NASA GEOS modeling system. J. Adv. Model. ~~EarthSyst~~Earth Syst., 10, 1266–1289, https://doi.org/10.1029/2017MS001251, 2018.

Freitas, S. R., Grell, G. A., and Li, H.: The Grell–Freitas (GF) convection parameterization: recent developments, extensions, and applications, Geosci. Model Dev., 14, 5393–5411, https://doi.org/10.5194/gmd-14-5393-2021, 2021.

Germe, A., Chevallier, M., y Mélia, D. S., Sanchez-Gomez, E., and Cassou, C.: Interannual predictability of Arctic sea ice in a global climate model: Regional contrasts and temporal evolution. Climate Dynamics, 43(9-10), 2519–2538, 2014.

Grell, G. A., and Freitas, S.: A scale and aerosol aware stochastic convective parameterization for weather and air quality modeling. Atmos. Chem. Phys., 14, 5233–5250, https://doi.org/10.5194/acp-14-5233-2014, 2014.

Guemas, V., Blanchard-Wrigglesworth, E., Chevallier, M., Day, J. J., Déqué, M., Doblas-Reyes, F. J., et al.: A review on Arctic sea-ice predictability and prediction on seasonal to decadal time-scales. Quarterly Journal of the Royal Meteorological Society, 142(695), 546–561, 2016.

Haidvogel, D. B., Arango, H., Budgell, W. P., Cornuelle, B. D., Curchitser, E., Di Lorenzo, E., et al.: Ocean forecasting in terrain-following coordinates: Formulation and skill assessment of the Regional Ocean Modeling System, Journal of Computational Physics, 227, 3595–3624, 2008.

Hecht, M. W., Wingate, B. A., and Kassis, P.: A better, more discriminating test problem for ocean tracer transport. Ocean Modell. 2 (1–2), 1–15. https://doi.org/10.1016/S1463-5003(00)00004-4, 2000.

Hersbach, H., Bell, B., Berrisford, P., et al.: The ERA5 global reanalysis. Quarterly Journal of the Royal Meteorological Society, 146, 1999-2049. https://doi.org/10.1002/qj.3803, 2020.

~~Hunt, B. R., Kostelich, E. J., Szunyogh, I.: Efficient data assimilation for spatiotemporal chaos: A local ensemble transform Kalman filter. Physica D 230: 112–126, 2007.~~

Horvat, C., and Tziperman, E.: A prognostic model of the sea-ice floe size and thickness distribution. Cryosphere 9, 2119–2134, 2015.

Horvat, C., Tziperman, E., and Campin, J.-M.: Interaction of sea ice floe size, ocean eddies, and sea ice melting. Geophysical Research Letters, 43, 8083–8090. https://doi.org/10.1002/2016GL069742, 2016.

Huang, Y., Chou, G., Xie, Y., & Soulard, N.: Radiative control of the interannual variability of Arctic sea ice. Geophysical Research Letters, 46, 9899– 9908. https://doi.org/10.1029/2019GL084204, 2019.

Itoh, M., Nishino, S., Kawaguchi, Y., and Kikuchi, T.: Barrow Canyon volume, heat, and freshwater fluxes revealed by long-term mooring observations between 2000 and 2008. J. Geophys. Res. Oceans, 118, 4363–4379, https://doi.org/10.1002/jgrc.20290, 2013.

Jung, T., Gordon, N.D., Bauer, P., Bromwich, D.H., Chevallier, M., Day, J.J., Dawson, J., Doblas-Reyes, F., Fairall, C., Goessling, H.F., Holland, M., Inoue, J., Iversen, T., Klebe, S., Lemke, P., Losch, M., Makshtas. A., Mills, B., Nurmi, P., Perovich, D., Reid, P., Renfrew, I.A., Smith, G., Svensson, G., Tolstykh, M., and Yang, Q.: Advancing Polar Prediction Capabilities on Daily to Seasonal Time Scales. Bulletin of the American Meteorological Society. https://doi.org/10.1175/BAMS-D-14-00246.1, 2016.

Kaleschke, L., Tian-Kunze, X., Maaß, N., Mäkynen, M., and Drusch, M.: Sea ice thickness retrieval from SMOS brightness temperatures during the Arctic freeze-up period. Geophys. Res. Lett., L05501, https://doi.org/10.1029/2012GL050916, 2012.

Kapsch, M., Graversen, R. G., Tjernström, M., and Bintanja, R.: The Effect of Downwelling Longwave and Shortwave Radiation on Arctic Summer Sea Ice. Journal of Climate 29, 3, 1143-1159, https://doi.org/10.1175/JCLI-D-15-0238.1, 2016.

Kay, J. E., L'Ecuyer, T., Gettelman, A., Stephens, G., and O'Dell, C.: The contribution of cloud and radiation anomalies to the 2007 Arctic sea ice extent minimum, Geophys. Res. Lett., 35, L08503, doi:10.1029/2008GL033451, 2008.

Keen, A., Blockley, E., Bailey, D. A., Boldingh Debernard, J., Bushuk, M., Delhaye, S., Docquier, D., Feltham, D., Massonnet, F., O'Farrell, S., Ponsoni, L., Rodriguez, J. M., Schroeder, D., Swart, N., Toyoda, T., Tsujino, H., Vancoppenolle, M., and Wyser, K.: An inter-comparison of the mass budget of the Arctic sea ice in CMIP6 models, The Cryosphere, 15, 951–982, https://doi.org/10.5194/tc-15-951-2021, 2021.

Kirkman, C. H., IV, and Bitz, C. M.: The Effect of the Sea Ice Freshwater Flux on Southern Ocean Temperatures in CCSM3: Deep-Ocean Warming and Delayed Surface Warming. Journal of Climate 24, 9, 2224-2237, https://doi.org/10.1175/2010JCLI3625.1, 2011.

Kwok, R.: Arctic sea ice thickness, volume, and multiyear ice coverage: Losses and coupled variability (1958–2018). Environmental Research Letters, 13(10), 105005, 2018

Laxon, S., Giles, K. A., Ridout, A. L., Wingham, D. J., Willatt, R., Cullen, R., Kwok, R., Schweiger, A., Zhang, J., Haas, C., Hendricks, S., Krishfield, R., Kurtz, N., Farrell, S., and Davidson, M.: CryoSat-2 estimates of Arctic sea ice thickness and volume, Geophys. Res. Lett., 40, https://doi.org/10.1002/grl.50193, 2013.

Lemieux, J. F., Dupont, F., Blain, P., Roy, F., Smith, G. C., and Flato, G. M.: Improving the simulation of landfast ice by combining tensile strength and a parameterization for grounded ridges. J. Geophys. Res. Oceans, 121:7354–7368, http://dx.doi.org/10.1002/2016JC012006, 2016.

Leonard, B., Mokhtari, S.: ULTRA-SHARP Non oscillatory Convection Schemes for High-Speed Steady Multidimensional Flow. Technical Report. NASA, 1990.

Liang, X., and Losch, M.: On the effects of increased vertical mixing on the Arctic Ocean and sea ice. Journal of Geophysical Research: Oceans, 123, 9266– 9282. https://doi.org/10.1029/2018JC014303, 2018.

Liu, J., Song, M., Horton, R., and Hu, Y.: Revisiting the potential of melt pond fraction as a predictor for the seasonal Arctic sea ice minimum. Environmental Research Letters, 10, 054017. https://doi.org/10.1088/1748-9326/10/5/054017, 2015.

Liu, J., Chen, Z., Hu, Y., Zhang, Y., Ding, Y., Cheng, X., et al.: Towards reliable arctic sea ice prediction using multivariate data assimilation. Science Bulletin, 64(1), 63–72, 2019.

Merryfield, W., Lee, W.-S., Wang, W., Chen, M., and Kumar, A.: Multi-system seasonal predictions of Arctic sea ice. Geophysical Research Letters, 40, 1551–1556. https://doi.org/10.1002/grl.50317, 2013.

Mallett, R. D. C., Stroeve, J. C., Cornish, S. B. Crawford, A. D., Lukovich, J. V., Serreze, M. C., Barrett, A. P., Meier, W. N., Heorton, H. D. B. S., and Tsamados, M.: Record winter winds in 2020/21 drove exceptional Arctic sea ice transport. Commun Earth Environ 2, 149, https://doi.org/10.1038/s43247-021-00221-8, 2021.

Maslanik, J. and Stroeve, J.: Near-Real-Time DMSP SSMIS Daily Polar Gridded Sea Ice Concentrations, Version 1. Boulder, Colorado USA. NASA National Snow and Ice Data Center Distributed Active Archive Center. https://doi.org/10.5067/U8C09DWVX9LM, 1999.

McLaughlin, F. A., Carmack, E. C., Williams, W. J., Zimmerman, S., Shimada, K., and Itoh, M.: Joint effects of boundary currents and thermohaline intrusions on the warming of

Atlantic water in the Canada Basin, 1993–2007. J. Geophys. Res., 114, C00A12, https://doi.org/10.1029/2008JC005001, 2009.

Meehl, G.A., Stocker, T. F., Collins, W. D., et al.: Global Climate Projections. In: Climate Change 2007: The Physical Science Basis. Contribution of Working Group I to the Fourth Assessment Report of the Intergovernmental Panel on Climate Change [Solomon, S., D. Qin, M. Manning, Z. Chen, M. Marquis, K.B. Averyt, M. Tignor and H.L. Miller (eds.)]. Cambridge University Press, Cambridge, United Kingdom and New York, NY, USA, 2007.

Msadek, R., Vecchi, G., Winton, M., and Gudgel, R.: Importance of initial conditions in seasonal predictions of Arctic sea ice extent. Geophysical Research Letters, 41, 5208–5215. https://doi.org/10.1002/2014GL060799, 2014.

Nakanishi, M., and Niino., H.: Development of an improved turbulence closure model for the atmospheric boundary layer. J. Meteor. Soc. Japan, 87, 895–912, https://doi.org/10.2151/jmsj.87.895, 2009.

~~Nerger,~~Naughten, K. A., Galton-Fenzi, B. K., Meissner, K. J., England, M. H., Brassington, G. B., Colberg, F., Hattermann, T., and Debernard, J. B.: Spurious sea ice formation caused by oscillatory ocean tracer advection schemes. Ocean Model., 116, 108–117, 2017.

Naughten, K. A., Meissner, K. J., Galton-Fenzi, B. K., England, M. H., Timmermann, R., Hellmer, H. H., Hattermann, T., and Debernard, J. B.: Intercomparison of Antarctic ice-shelf, ocean, and sea-ice interactions simulated by MetROMS-iceshelf and FESOM 1.4. Geosci. Model. Dev., 11, 1257–1292, 2018

~~L., Danilov, S., Hiller, W., Schröter, J.: Using sea-level data to constrain a finite-element primitive-equation ocean model with a local SEIK filter, Ocean Dynamics, 56(5/6), 634-649., https://doi.org/10.1007/s10236-006-0083-0, 2006.~~

Nerger, L., and Hiller, W.: Software for Ensemble-based Data Assimilation Systems - Implementation Strategies and Scalability. Computers and Geosciences, 55, 110-118. https://doi.org/10.1016/j.cageo.2012.03.026, 2013.

Nerger, L., Janjić, T., Schröter, J. and Hiller, W.: A unification of ensemble square root Kalman filters. Monthly Weather Review, 140, 2335-2345. https://doi.org/10.1175/MWR-D-11-00102.1, 2012.

Newton, R., Pfirman, S., Schlosser, P., Tremblay, B., Murray, M. and Pomerance, R.: White Arctic vs. Blue Arctic: A case study of diverging stakeholder responses to environmental change. Earth's Future, 4: 396-405. https://doi.org/10.1002/2016EF000356, 2016.

Nicolaus M., Katlein, C., Maslanik, J., and Hendricks, S.: Changes in Arctic sea ice result in increasing light transmittance and absorption. Geophysical Research Letters, 39, L24501. https://doi.org/10.1029/2012GL053738, 2012

Nicolaus M., and Katlein, C.: Mapping radiation transfer through sea ice using a remotely operated vehicle (ROV). The Cryosphere, 7, 763-77. https://doi.org/10.5194/tc-7-763-2013, 2013.

Notz, D., Jahn, A., Holland, M., Hunke, E., Massonnet, F., Stroeve, J., Tremblay, B., and Vancoppenolle, M.: The CMIP6 Sea-Ice Model Intercomparison Project (SIMIP): understanding sea ice through climate-model simulations, Geosci. Model Dev., 9, 3427–3446, https://doi.org/10.5194/gmd-9-3427-2016, 2016.

Ogi, M., Yamazaki, K., and Wallace, J. M.: Influence of winter and summer surface wind anomalies on summer Arctic sea ice extent, Geophys. Res. Lett., 37, L07701, doi:10.1029/2009GL042356, 2010.

Olonscheck, D., Mauritsen, T. and Notz, D.: Arctic sea-ice variability is primarily driven by atmospheric temperature fluctuations. Nat. Geosci. 12, 430–434, https://doi.org/10.1038/s41561-019-0363-1, 2019.

Padman, L., and Dillon, T. M.: Vertical heat fluxes through the Beaufort Sea thermohaline staircase. J. Geophys. Res., 92, 10 799–10 806, https://doi.org/10.1029/JC092iC10p10799, 1987.

Perovich, D., Richter-Menge, J., Jones, K., Light, B., Elder, B., Polashenski, C., Laroche, D., Markus, T., and Lindsay, R.: Arctic sea-ice melt in 2008 and the role of solar heating. Annals of Glaciology, 52(57), 355-359. doi:10.3189/172756411795931714, 2011.

Perovich, D., Richter-Menge, J., Polashenski, C., Elder, B., Arbetter, T., and Brennick, O.: Sea ice mass balance observations from the North Pole Environmental Observatory, Geophys. Res. Lett., 41, 2019– 2025, doi:10.1002/2014GL059356, 2014.

Peterson, K., Arribas, A., Hewitt, H., Keen, A., Lea, D., and McLaren, A.: Assessing the forecast skill of Arctic sea ice extent in the GloSea4 seasonal prediction system. Climate Dynamics, 44(1-2), 147–162, 2015.

Pham, D. T.: Stochastic methods for sequential data assimilation in strongly nonlinear systems. Mon. Wea. Rev., 129, 1194–1207, 2001.

Rasch, P. J.: Conservative shape-preserving two-dimensional transport on a spherical reduced grid, Mon. Wea. Rev, 122, 1337-1350, 1994.

Reynolds, R. W., Smith, T. M., Liu, C., Chelton, D. B., Casey, K. S., and Schlax, M. G.: Daily High-Resolution-Blended Analyses for Sea Surface Temperature, Journal of Climate, 20(22), 5473-5496, 2007.

Ricker, R., Hendricks, S., Kaleschke, L., Tian-Kunze, X., King, J., and Haas, C.: A weekly Arctic sea-ice thickness data record from merged CryoSat-2 and SMOS satellite data, The Cryosphere, 11, 1607–1623, https://doi.org/10.5194/tc-11-1607-2017, 2017.

Roach, L. A., Bitz, C. M., Horvat, C., and Dean, S. M.: Advances in modeling interactions between sea ice and ocean surface waves. Journal of Advances in Modeling Earth Systems, 11. https://doi.org/10.1029/2019MS001836, 2019.

Roach, L. A., Horvat, C., Dean, S. M., and Bitz, C. M.: An emergent sea ice floe size distribution in a global coupled ocean–sea ice model. Journal of Geophysical Research: Oceans, 123(6), 4322–4337. https://doi.org/10.1029/2017JC013692, 2018.

Rocheta, E., Evans, J. P., and Sharma, A.: Can Bias Correction of Regional Climate Model Lateral Boundary Conditions Improve Low-Frequency Rainfall Variability?, Journal of Climate, 30(24), 9785-9806, 2017.

Rocheta, E., Evans, J. P. and Sharma, A.: Correcting lateral boundary biases in regional climate modelling: the effect of the relaxation zone. Clim. Dyn., 55, 2511–2521. https://doi.org/10.1007/s00382-020-05393-1, 2020.

Serreze, M. C. and Meier, W. N.: The Arctic's sea ice cover: trends, variability, predictability, and comparisons to the Antarctic. Ann. N.Y. Acad. Sci., 1436: 36-53. https://doi.org/10.1111/nyas.13856, 2019.

Saha, S., Moorthi, S., Wu, X., et al.: The NCEP climate forecast system version 2. J. Clim. 27:2185–2208, 2014.

Schmidt, G. A., Bitz, C. M., Mikolajewicz, U., and Tremblay, L.-B.: Ice–ocean boundary conditions for coupled models, Ocean Model., 7, 59–74, 2004.

Shchepetkin, A.F., McWilliams, J. C.: Quasi-monotone advection schemes based on explicit locally adaptive dissipation. Mon. Weather Rev. 126 (6), 1541–1580, 1998.

Shchepetkin, A. F., and McWilliams, J. C.: The Regional Ocean Modeling System: A split-explicit, free-surface, topography following coordinates ocean model, Ocean Modelling, 9, 347-404, 2005.

Shi, X., Notz, D., Liu, J., Yang, H., and Lohmann, G.: Sensitivity of Northern Hemisphere climate to ice–ocean interface heat flux parameterizations, Geosci. Model Dev., 14, 4891–4908, https://doi.org/10.5194/gmd-14-4891-2021, 2021.

Sigmond, M., Fyfe, J., Flato, G., Kharin, V., and Merryfield, W.: Seasonal forecast skill of Arctic sea ice area in a dynamical forecast system. Geophysical Research Letters, 40, 529–534. https://doi.org/10.1002/grl.50129, 2013.

Skamarock, W. C., Klemp, J. B., Dudhia, J., Gill, D. O., Barker, D. M., Wang, W. and Powers, J. G.: A Description of the Advanced Research WRF Version 2. NCAR Technical Note, NCAR/TN-468+STR, 2005.

Smolarkiewicz, P. K.: Multidimensional positive definite advection transport algorithm: An overview. Int. J. Numer. Methods Fluids, 50, 1123–1144, 2006.

Song, Y. and Haidvogel, D. B.: A semi-implicit ocean circulation model using a generalized topography-following coordinate system. J. Comp. Phys., 115(1), 228-244, 1994.

Steele, M.: Sea ice melting and floe geometry in a simple ice-ocean model. Journal of Geophysical Research: Oceans, 97(C11), 17,729–17,738. https://doi.org/10.1029/92JC01755, 1992.

Stroeve, J., Blanchard-Wrigglesworth, E., Guemas, V., Howell, S., Massonnet, F., and Tietsche, S.: Improving predictions of Arctic sea ice extent, Eos, 96, https://doi.org/10.1029/2015EO031431, 2015.

Stroeve, J., Hamilton, L. C., Bitz, C. M., and Blanchard-Wrigglesworth, E.: Predicting September sea ice: Ensemble skill of the SEARCH Sea Ice Outlook 2008 – 2013, Geophys. Res. Lett., 41, 2411-2418, https://doi.org/10.1002/2014GL059388, 2014.

Tian-Kunze, X., Kaleschke, L., Maaß, N., Mäkynen, M., Serra, N., Drusch, M., and Krumpen, T.: SMOS-derived thin sea ice thickness: Algorithm baseline, product specifications and initial verification. Cryosphere, 8, 997-1018, https://doi.org/10.5194/tc-8-997-2014, 2014.

Tietsche, S., Day, J., Guemas, V., Hurlin, W., Keeley, S., Matei, D., et al.: Seasonal to interannual Arctic sea ice predictability in current global climate models. Geophysical Research Letters, 41, 1035–1043. https://doi.org/10.1002/2013GL058755, 2014.

Tsamados, M., Feltham, D. L., and Wilchinsky, A. V.: Impact of a new anisotropic rheology on simulations of Arctic sea ice, J. Geophys. Res. Oceans, 118, 91–107, doi:10.1029/2012JC007990, 2013.

Turner, A. K., and Hunke, E. C.: Impacts of a mushy-layer thermodynamic approach in global sea-ice simulations using the CICE sea-ice model, J. Geophys. Res. Oceans, 120, 1253-1275, doi:10.1002/2014JC010358, 2015.

Turner, A. K., Hunke, E. C., and Bitz, C. M.: Two modes of sea-ice gravity drainage: A parameterization for large-scale modeling, J. Geophys. Res., 118, 2279–2294, doi:10.1002/jgrc.20171, 2013.

Turner, J. S.: Buoyancy Effects in Fluids. Cambridge University Press, 368 pp. 1973.

Van den Dool, H.: Empirical Methods in Short-Term Climate Prediction, Oxford Univ. Press, Oxford, U. K., 2006.

Wang, W., Chen, M., and Kumar, A.: Seasonal prediction of Arctic sea ice extent from a coupled dynamical forecast system. Monthly Weather Review, 141(4), 1375–1394, 2013.

Warner, J. C., Armstrong, B., He, R., and Zambon, J.: Development of a coupled ocean–atmosphere–wave–sediment transport (COAWST) modeling system. Ocean Modell. 35, 230–244, 2010.

Woodgate, R. A., Aagaard, K., and Weingartner, T. J.: A year in the physical oceanography of the Chukchi Sea: Moored measurements from autumn 1990–1991. Deep-Sea Res. II, 52, 3116–3149, https://doi.org/10.1016/j.dsr2.2005.10.016, 2005.

Wu, W., Lynch, A. H., and Rivers, A.: Estimating the Uncertainty in a Regional Climate Model Related to Initial and Lateral Boundary Conditions, Journal of Climate, 18(7), 917-933, 2005.

Yang, C.-Y., Liu, J., and Xu, S.: Seasonal Arctic sea ice prediction using a newly developed fully coupled regional model with the assimilation of satellite sea ice observations. Journal of Advances in Modeling Earth Systems, 12, e2019MS001938. https://doi.org/10.1029/2019MS001938, 2020.

Zampieri, L., Goessling, H. F., and Jung, T.: Bright prospects for Arctic sea ice prediction on subseasonal time scales. Geophysical Research Letters, 45, 9731– 9738. https://doi.org/10.1029/2018GL079394, 2018.

Zhang, J. and Rothrock, D.: Modeling global sea ice with a thickness and enthalpy distribution model in generalized curvilinear coordinates. Mon. Wea. Rev., 131, 845–861, 2003.

Zhang, J., Lindsay, R., Steele, M., and Schweiger, A.: What drove the dramatic retreat of arctic sea ice during summer 2007?, Geophys. Res. Lett., 35, L11505, doi:10.1029/2008GL034005, 2008.

Zhang, J., Schweiger, A., Steele, M., and Stern, H.: Sea ice floe size distribution in the marginal ice zone: Theory and numerical experiments. Journal of Geophysical Research: Oceans, 120, 3484–3498. https://doi.org/10.1002/2015JC010770, 2015.

Zhang, J., Stern, H., Hwang, B., Schweiger, A., Steele, M., Stark, M., and Graber, H. C.: Modeling the seasonal evolution of the Arctic sea ice floe size distribution. Elementa: Science of the Anthropocene, 4(1), 126. https://doi.org/10.12952/journal.elementa.000126, 2016.

7. Tables

~~Table 1 Difference in versions for the model components between the original and updated CAPS~~

	~~Yang et al. (2020)~~	~~This paper~~
~~COAWST~~	~~3.1~~	~~3.5~~
~~WRF~~	~~3.6.1~~	~~4.1.2~~
~~ROMS~~	~~3.7 revision 748~~	~~3.8 revision 981~~
~~CICE~~	~~5.1.2~~	~~6.0.0~~

~~Table 2~~Table 1 The summary of physic parameterizations used in the Y21_CRTL experiment

WRF physics	
Cumulus parameterization	Grell-Freitas (Freitas et al. 2018; improved from Y20)
Microphysics parameterization	Morrison 2-moment (Morrison et al. 2009; same as Y20)
Longwave radiation parameterization	CAM spectral band scheme (Collins et al. 2004; same as Y20)
Shortwave radiation parameterization	CAM spectral band scheme (Collins et al. 2004; same as Y20)
Boundary layer physics	MYNN2 (Nakanishi and Niino, 2006; improved from Y20)
Land surface physics	Unified Noah LSM (Chen and Dudhia, 2001; improved from Y20)
ROMS physics	
Tracer advection scheme	MPDATA (Smolarkiewicz, 2006; same as Y20)
Tracer vertical mixing scheme	GLS (Umlauf and Burchard, 2003; same as Y20)
Bottom drag scheme	Quadratic bottom friction (QDRAG;

	(same as Y20)
CICE physics	
Ice dynamics	EVP (Hunke and Dukowicz, 1997; improved from Y20)
Ice thermodynamics	Bitz and Lipscomb (1999; same as Y20)
Shortwave albedo	Delta-Eddington (Briegleb and Light, 2007; same as Y20)

Table ~~3~~2 The summary of the prediction experiments and details of experiment designs. Note: All experiments use the CFS operational forecasts as initial and boundary conditions; VT: vertical transformation function; VS: vertical stretching function; SH94: stretching function of Song and Haidvogel (1994); S10: stretching function of Shchepetkin (2010).

Experiment	Physics	Assimilation	ROMS vertical coordinate	Simulation period
~~Y20~~	~~Physics (old version) listed in Table 2~~	~~2 localization radii~~ ~~SSMIS SIC~~ ~~Simply-merged CryoSat-2/SMOS SIT~~	~~VT 1~~ ~~VS SH94~~ ~~h_c 10m~~	~~2018.07.01-2018.10.01~~
Y20_MOD	Physics (old version) listed in Table ~~2~~1	6 localization radii SSMIS SIC Simply-merged CryoSat-2/SMOS SIT	VT 1 VS SH94 h_c 10m	2018.07.01-2018.10.01
Y21_CTRL	Physics (new version) listed in Table ~~2~~1	6 localization radii SSMIS SIC Simply-merged CryoSat-2/SMOS SIT	VT 1 VS SH94 h_c 10m	2018.07.01-2018.10.01
Y21_VT	Physics (new version)	6 localization radii	VT 2	2018.07.01-

	listed in Table ~~2~~1	SSMIS SIC Simply-merged CryoSat-2/SMOS SIT	VS S10 h_c 300m	2018.10.01
Y21_RP	Advection: U3H/C4V ~~Bottom drag: LOGDRAG~~	6 localization radii SSMIS SIC Simply-merged CryoSat-2/SMOS SIT	VT 2 VS S10 h_c 300m	2018.07.01-2018.10.01
Y21_MUSHY	Same physics as Y21_RP CICE: Mushy layer thermodynamics	6 localization radii SSMIS SIC Simply-merged CryoSat-2/SMOS SIT	VT 2 VS S10 h_c 300m	2018.07.01-2018.10.01
Y21_ SIT	Same physics as Y21_RP	6 localization radii SSMIS SIC OI-merged CryoSat-2/SMOS SIT	VT 2 VS S10 h_c 300m	2018.07.01-2018.10.01
Y21_EXT-7	Same physics as Y21_RP	6 localization radii SSMIS SIC OI-merged CryoSat-2/SMOS SIT	VT 2 VS S10 h_c 300m	2018.07.01-2019.01.31
Y21_MAR-7	Same physics as	6 localization radii	VT 2	2018.03.01-

	Y21_RP	SSMIS SIC OI-merged CryoSat-2/SMOS SIT	VS S10 h_c 300m	2018.09.30

8. Figures

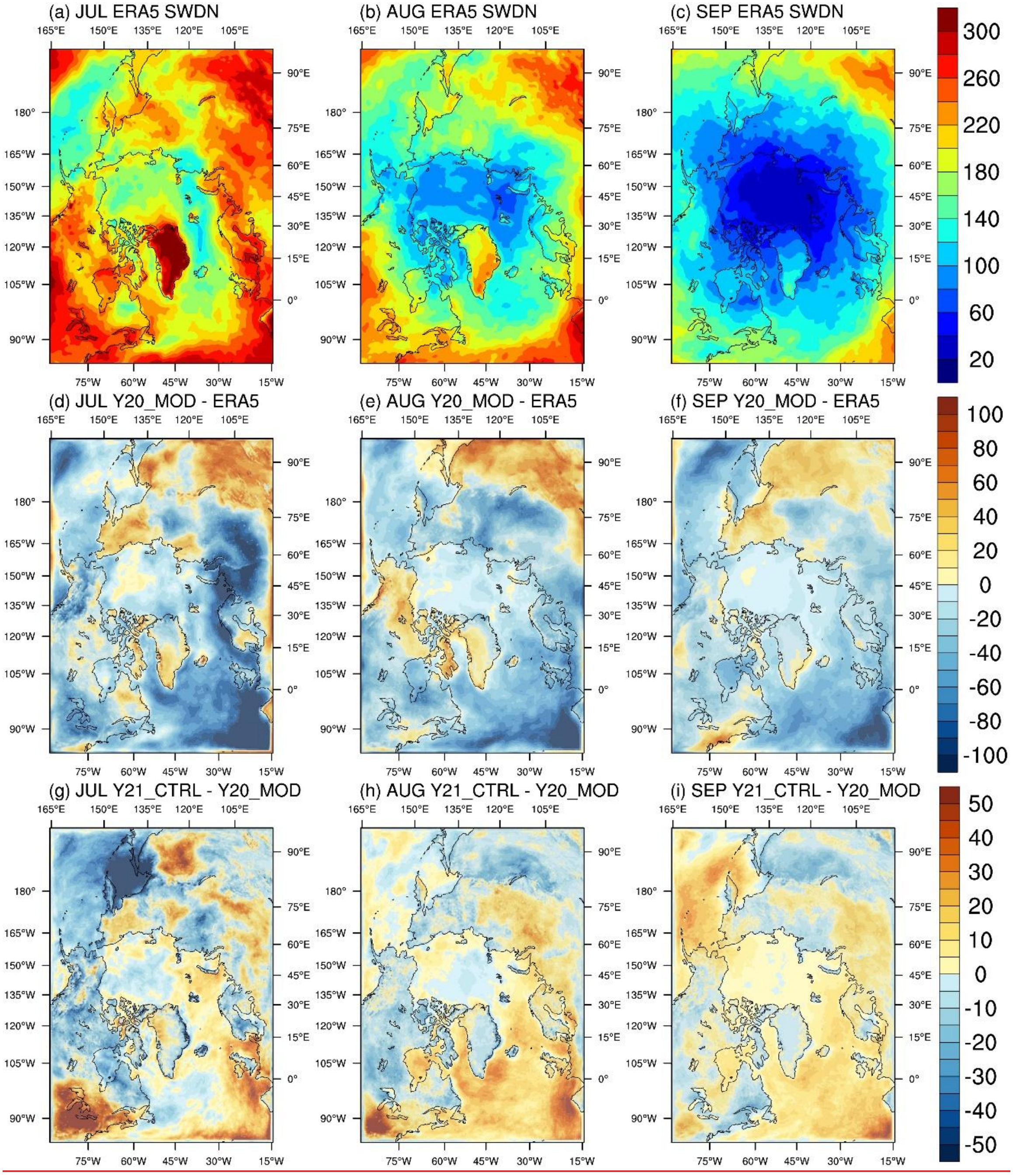

Figure 1 ERA5 monthly mean of downward shortwave radiation at the surface for (a) July, (b) August, and (c) September, the difference between Y20_MOD and ERA5 for (d) July, (e) August, (f) September, and the difference between Y21_CTRL and Y20_MOD for (g) July, (h) August, and (i) September.

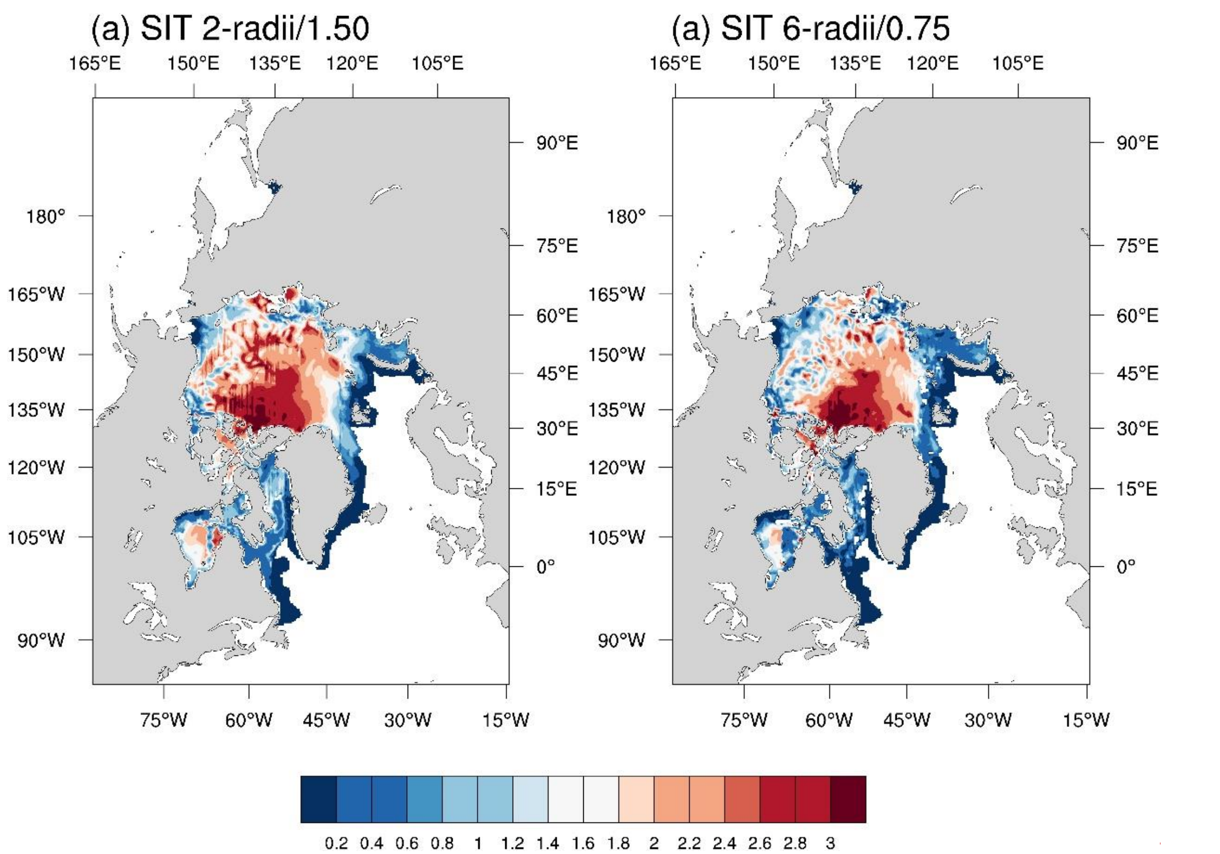

~~Figure 1 The initial sea ice thickness after data assimilation with (a) 2 localization radii/1.5m ice thickness uncertainty, and (b) 6 localization radii/0.75m ice thickness uncertainty.~~

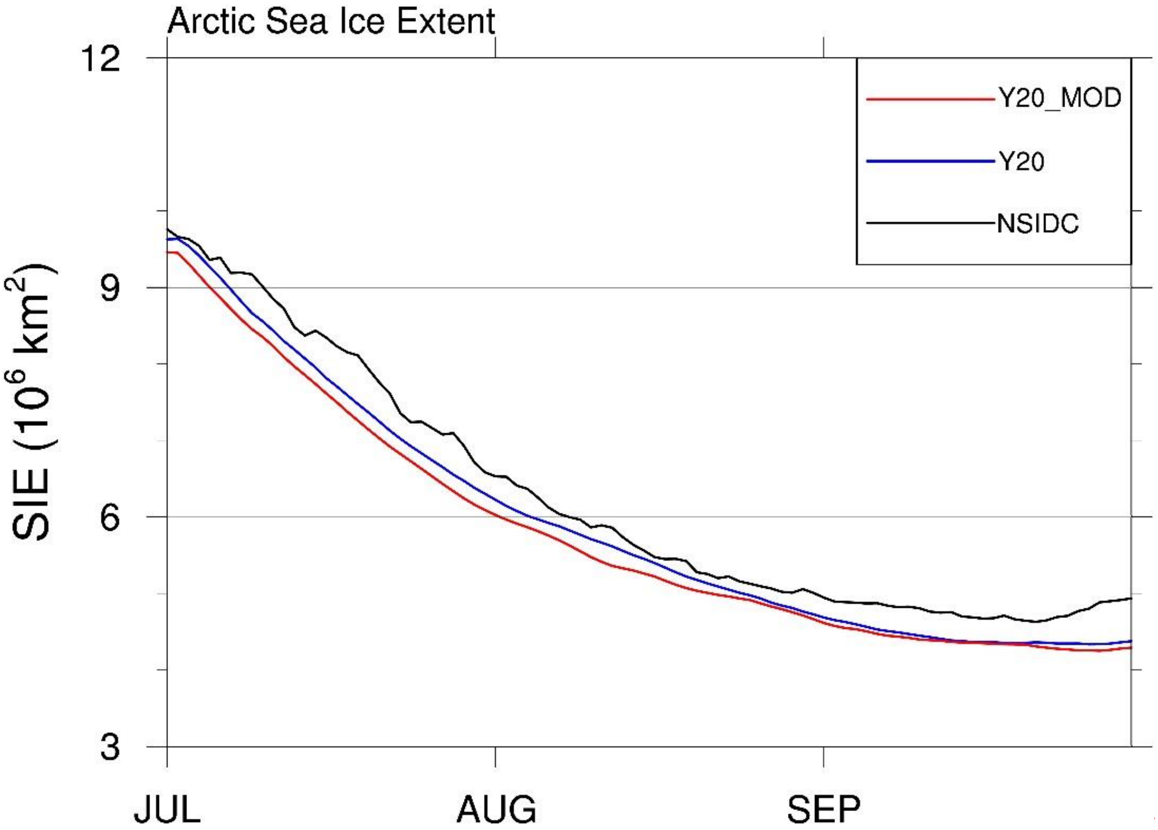

~~Figure 2 Time-series of Arctic sea ice extent for the observations (black line) and the ensemble mean of Y20 (blue line) and Y20_MOD (red line).~~

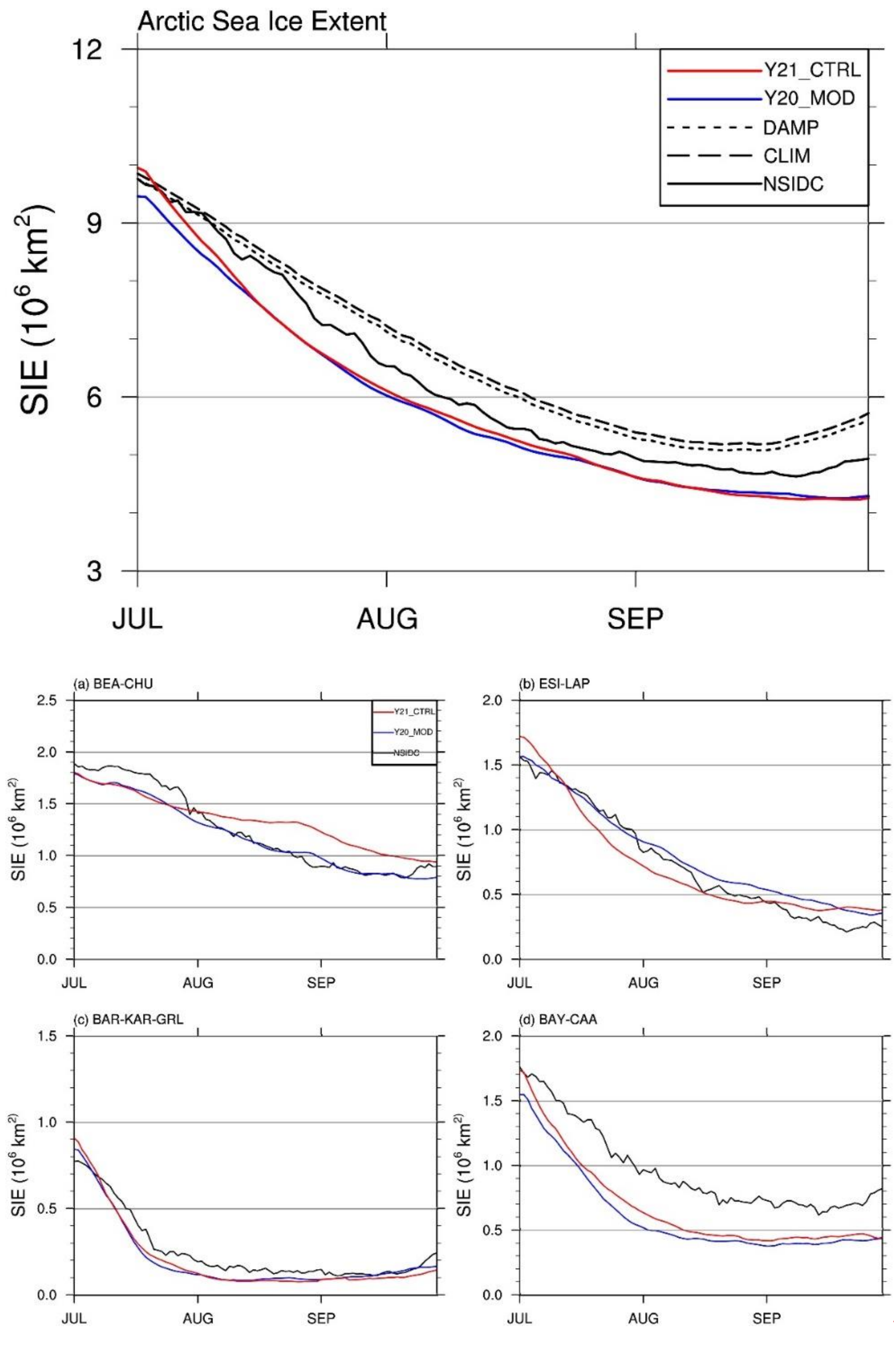
Arctic Sea Ice Extent
SIE (10^6 km^2)
Y21_CTRL
Y20_MOD
DAMP
CLIM
NSIDC
12
9
6
3
JUL
AUG
SEP
(a) BEA-CHU
(b) ESI-LAP
(c) BAR-KAR-GRL
(d) BAY-CAA

~~Figure 3~~

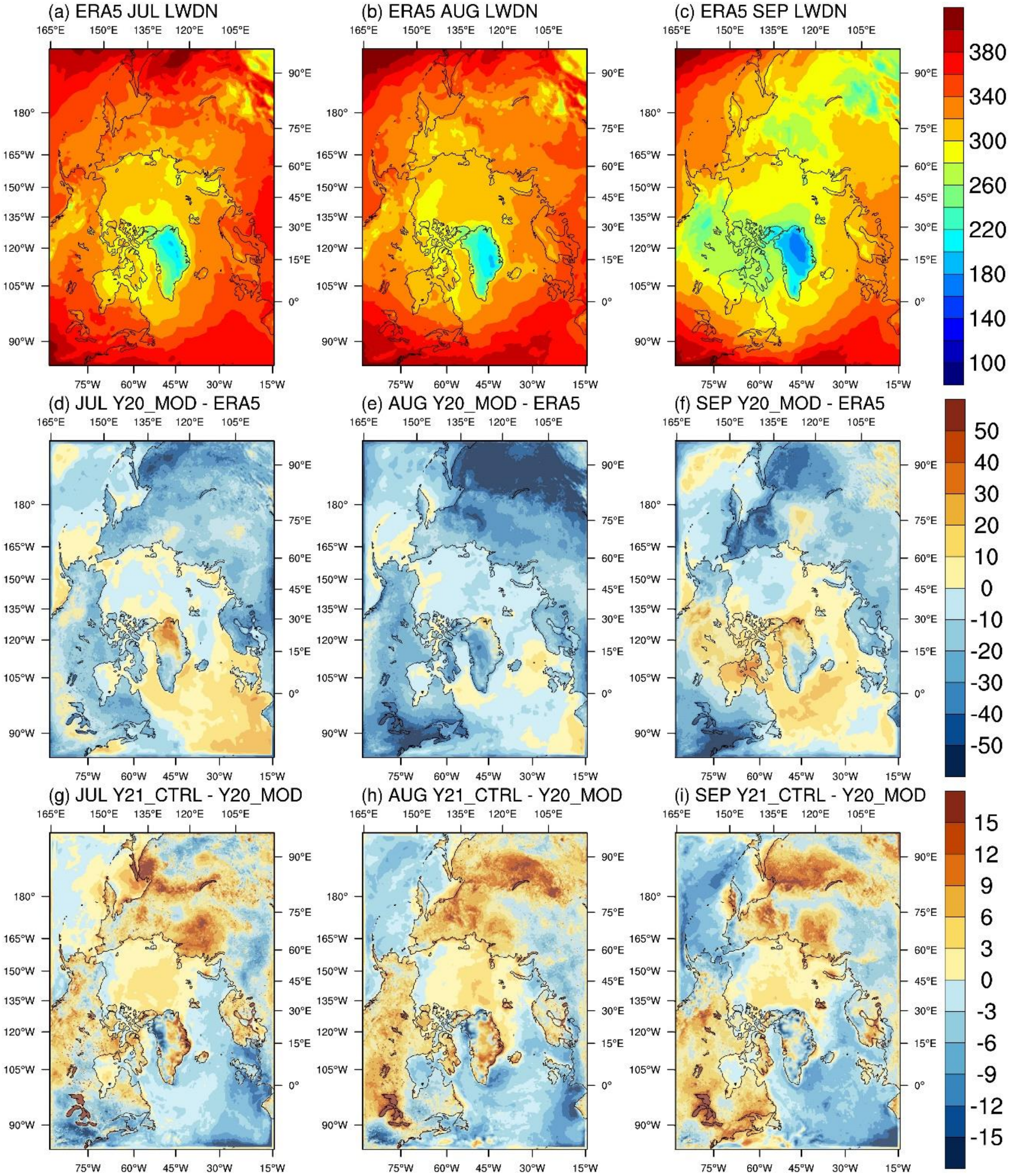

Figure 2 Same as Figure 1, but for downward thermal radiation at the surface.

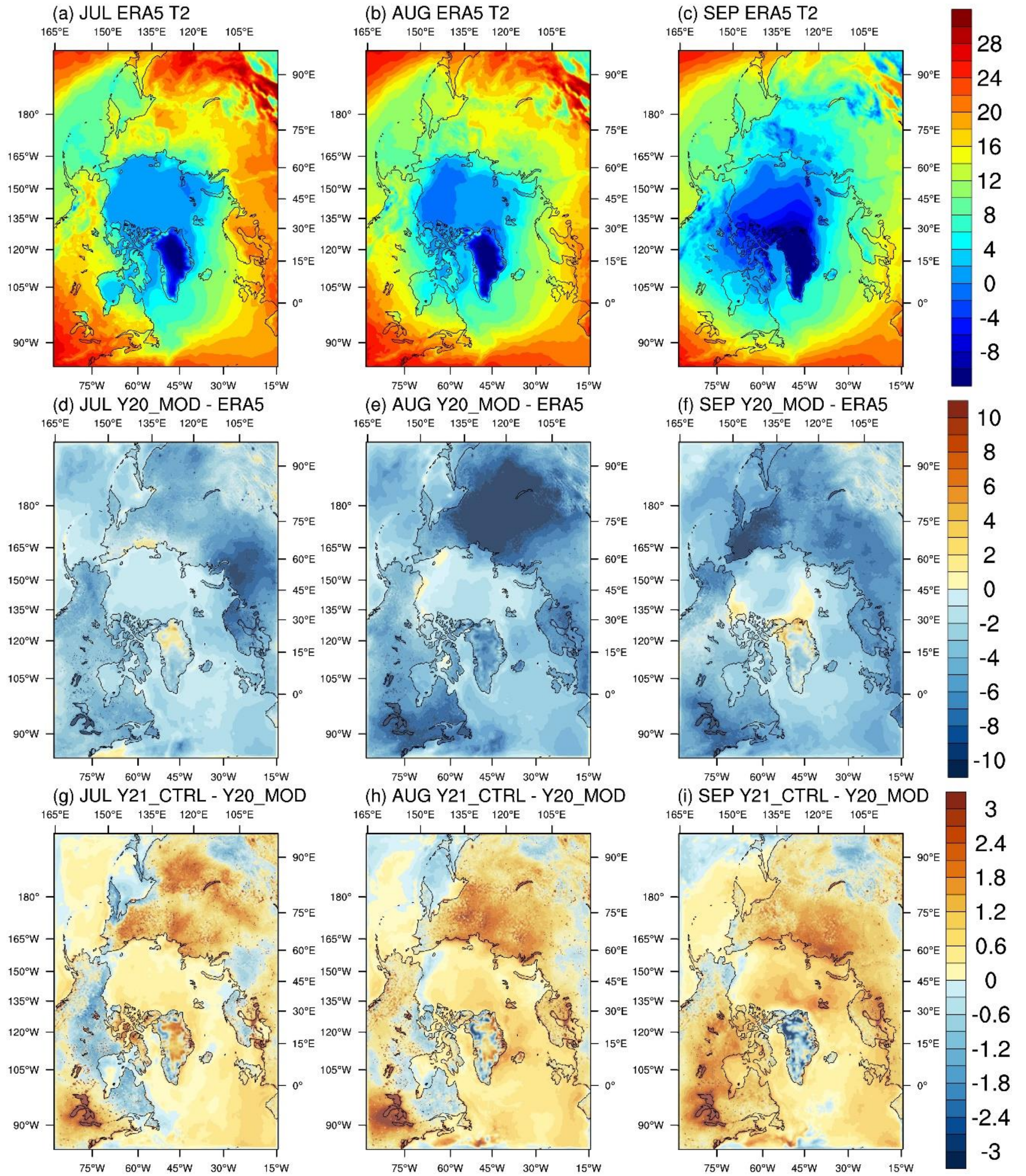

Figure 3 Same as Figure 1, but for near-surface air temperature.

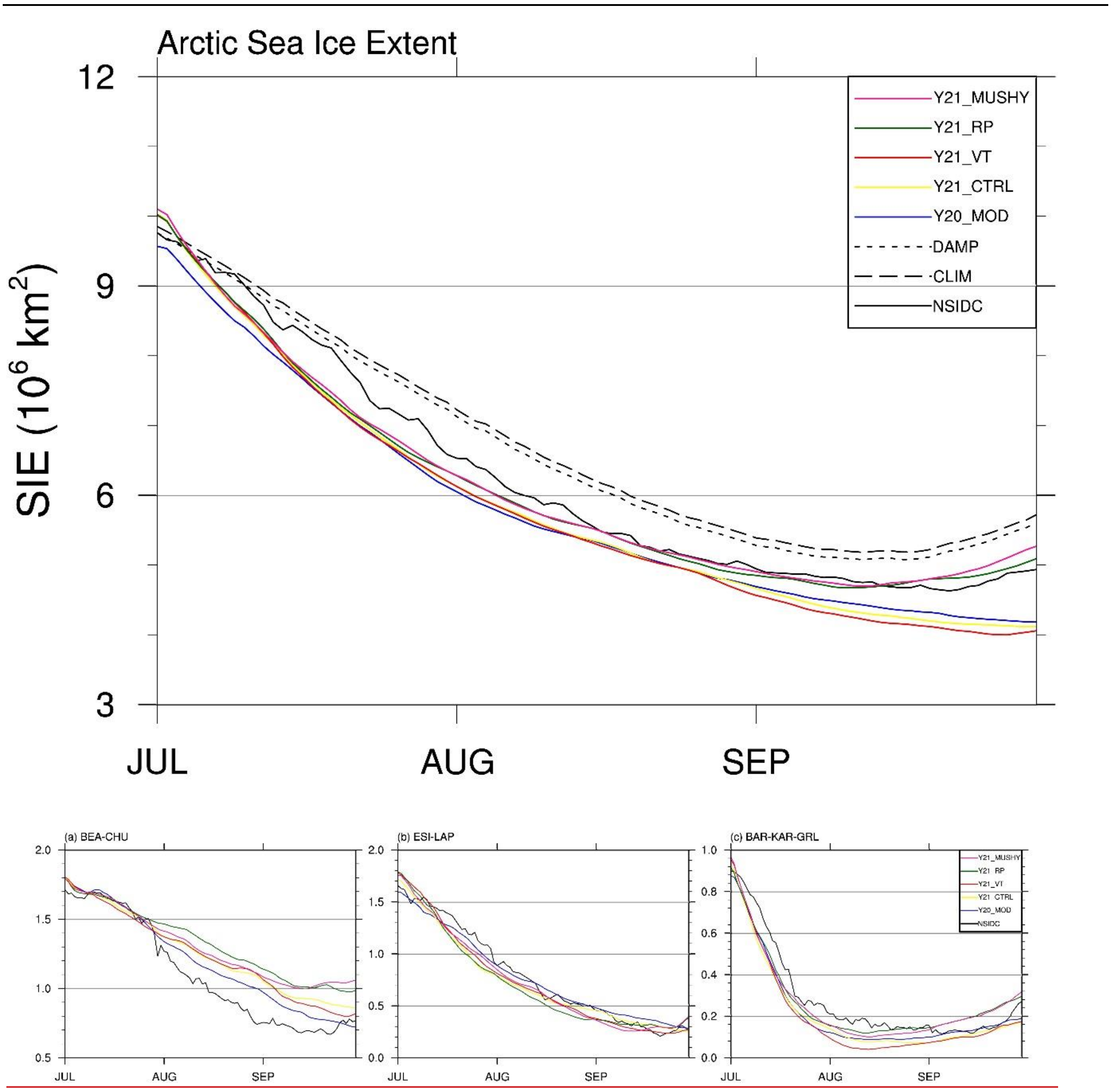

Figure 4 Top panel: Time-series of Arctic sea ice extent for the observations (black line) and the ensemble-mean of Y20_MOD (blue line~~) and~~), Y21_CTRL (yellow line), Y21_VT (red line), Y21_RP (green line), and Y21_MUSHY (pink line). Dashed and dotted lines are the climatology and the damped anomaly persistence predictions. Bottom panel: Time-series of the observed (black line) and the ensemble-mean of regional sea ice extents for Y20_MOD (blue line~~) and~~), Y21_CTRL (yellow line), Y21_VT (red line~~).~~), Y21_RP (green line), and Y21_MUSHY (pink line) for (a) Beaufort-Chukchi Seas, (b) East Siberian-Laptev Seas, and (c) Barents-Kara-Greenland Seas~~, and (d) Baffin Bay-Canadian Archipelago~~.

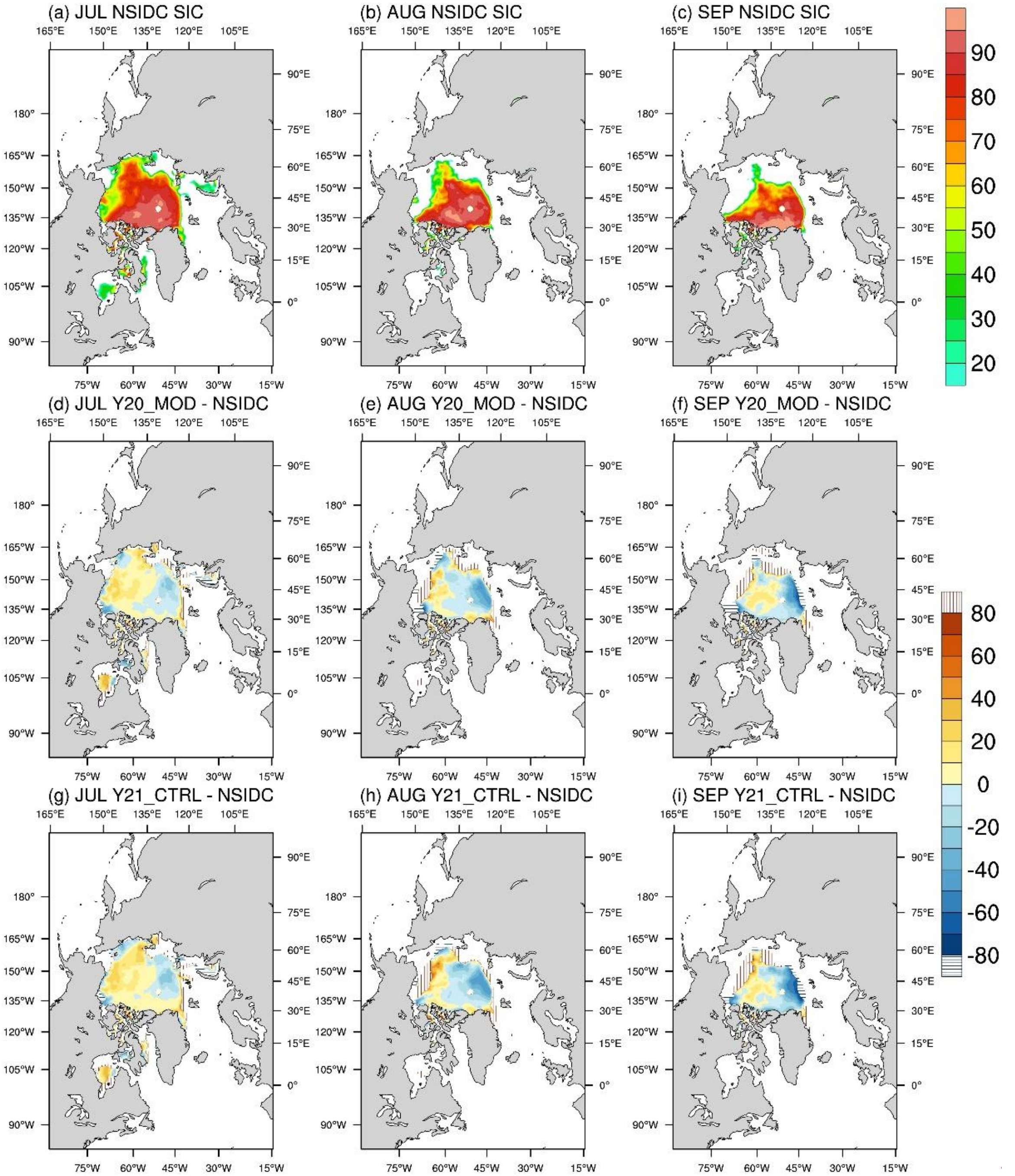
(a) JUL NSIDC SIC
(b) AUG NSIDC SIC
(c) SEP NSIDC SIC
90
80
70
60
50
40
30
20
(d) JUL Y20_MOD - NSIDC
(e) AUG Y20_MOD - NSIDC
(f) SEP Y20_MOD - NSIDC
80
60
40
20
0
-20
-40
-60
-80
(g) JUL Y21_CTRL - NSIDC
(h) AUG Y21_CTRL - NSIDC
(i) SEP Y21_CTRL - NSIDC

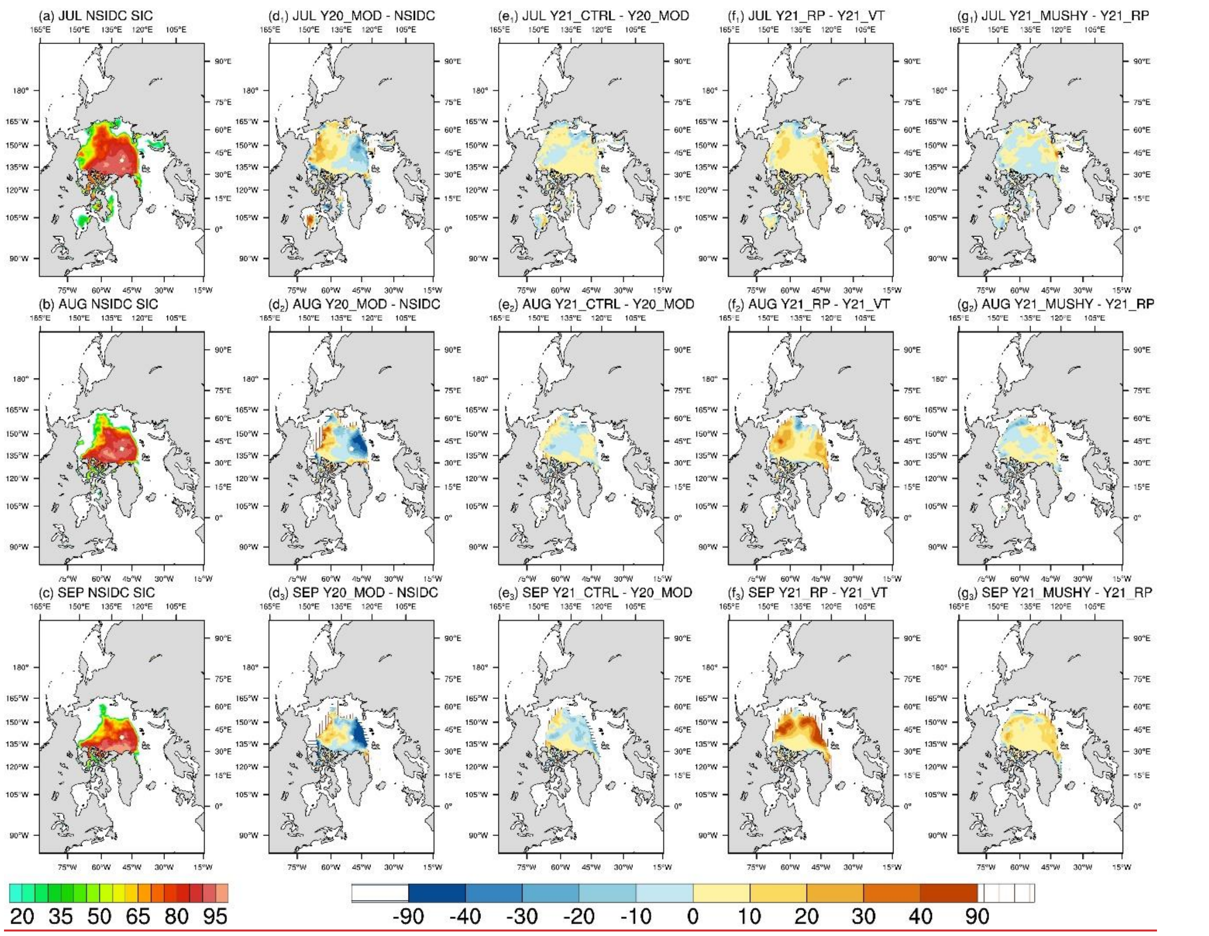

Figure ~~4~~5 Monthly mean of sea ice concentration for (a) July, (b) August, (c) September of the NSIDC observations, and the difference between the ~~predictions~~all prediction experiments and the observations for (~~d~~d_1-g_1) July, (~~e~~d_2-g_2) August, (~~f~~d_3-g_3) September~~ of Y20_MOD, (g) July, (h) August, and (i) September of Y21_CTRL~~. Vertical/horizontal-line areas represent the difference of ice edge location (15% concentration).

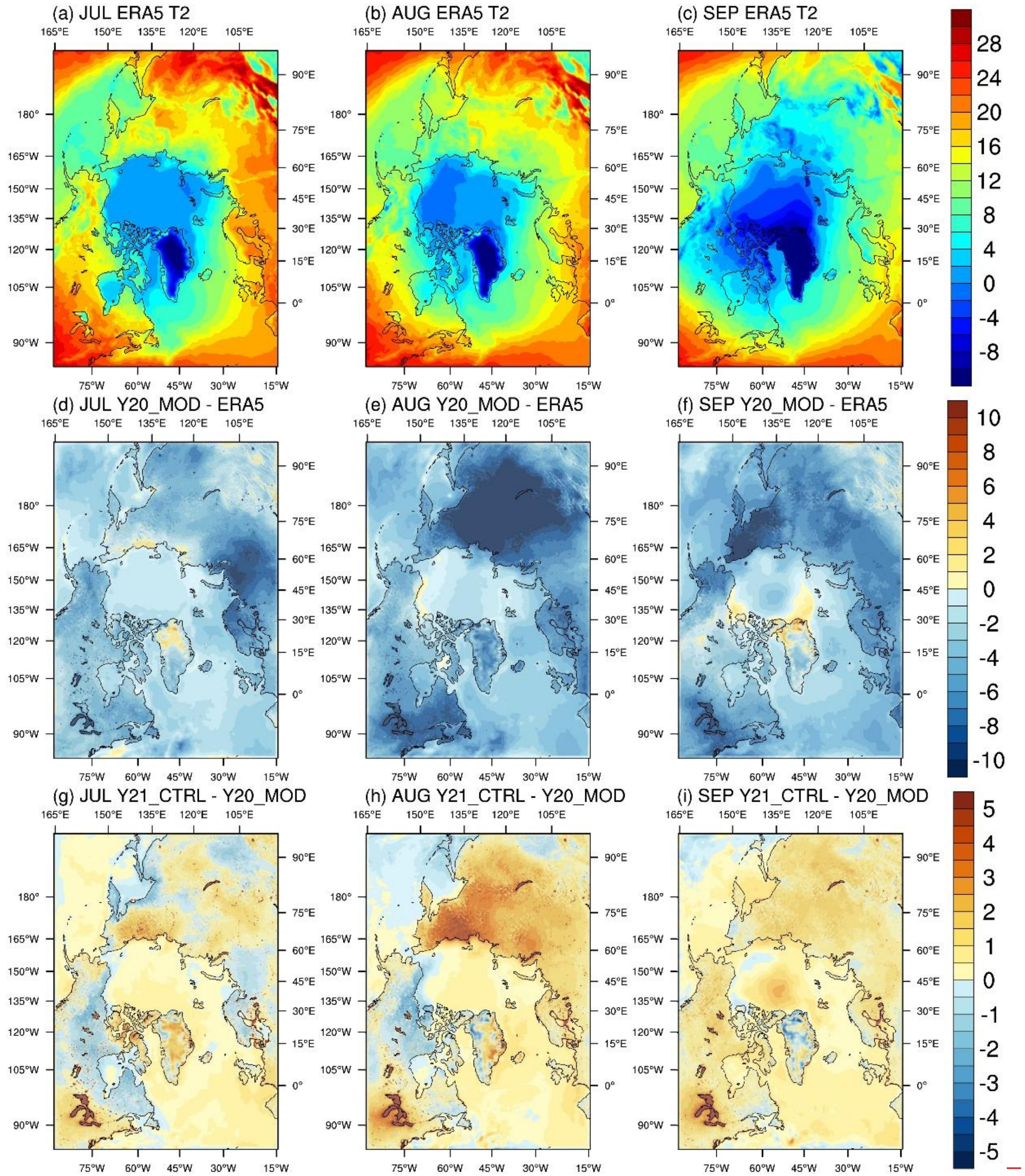

~~Figure 5 ERA5 monthly mean of near-surface air temperature~~

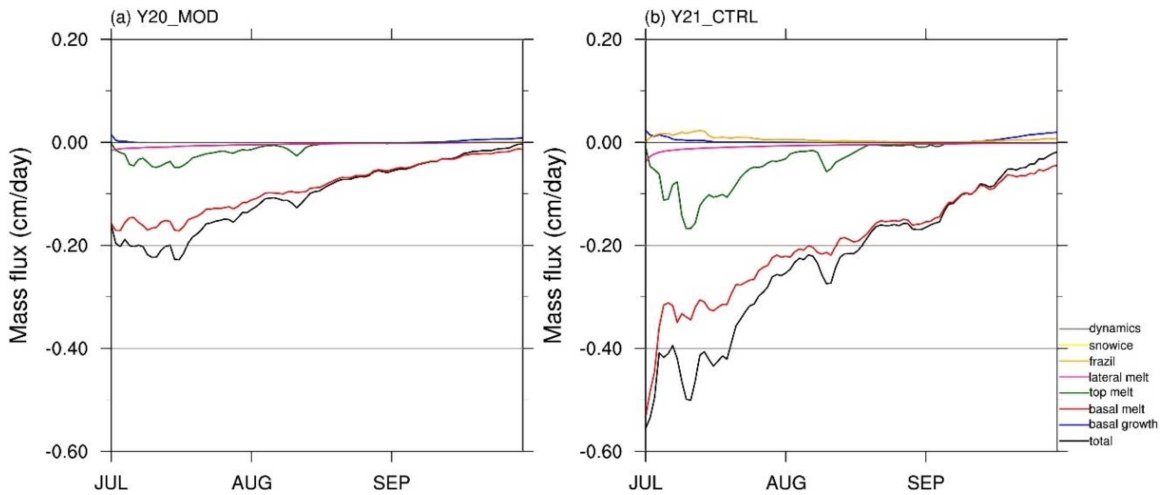

~~for (a) July, (b) August, and (c) September, the difference between Y20_MOD and ERA5 for (d) July, (e) August, (f) September, and the difference between Y21_CTRL and Y20_MOD for (g) July, (h) August, and (i) September.~~

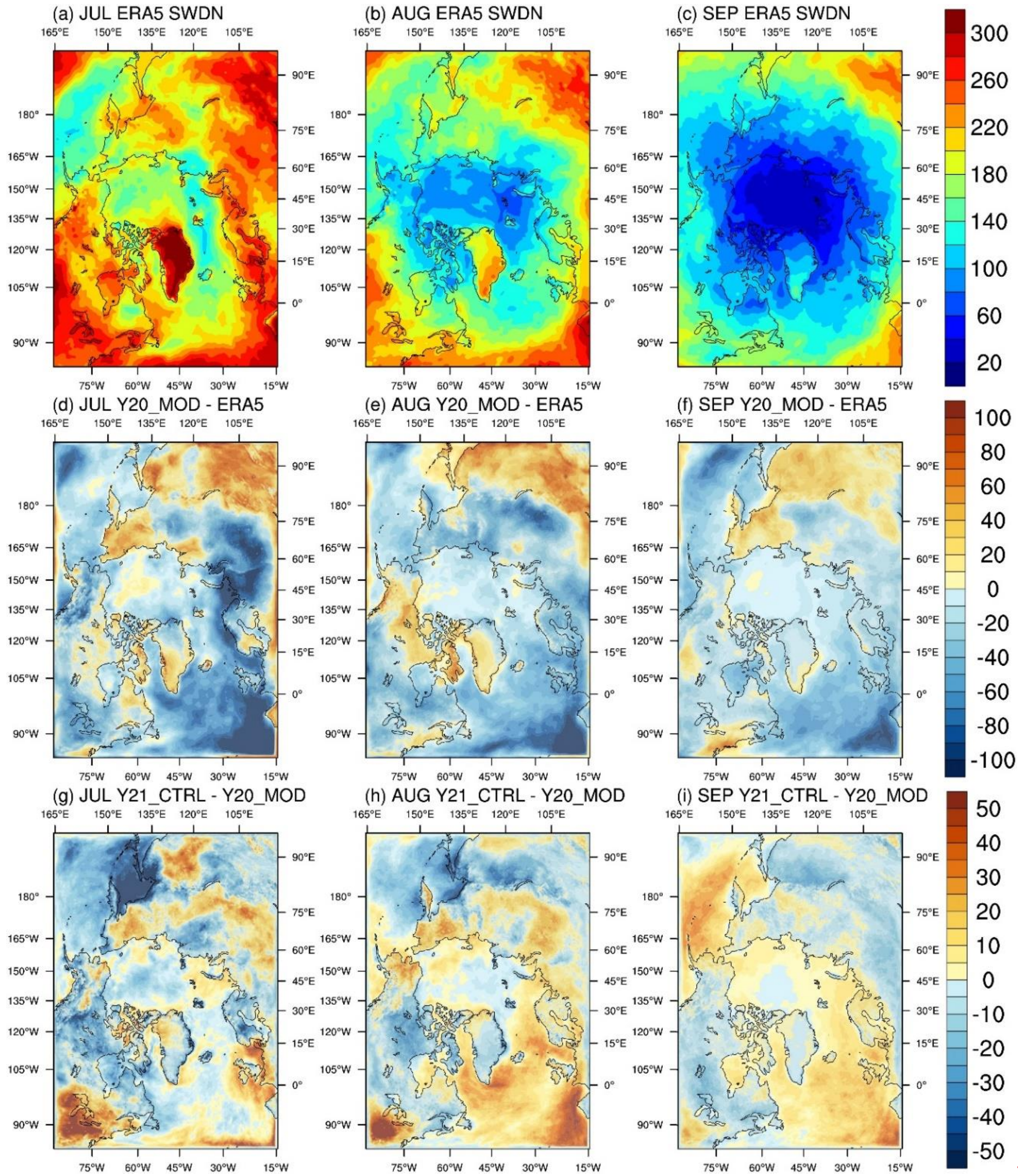

Figure 6 ~~Same as~~ Time-series of sea ice mass budget terms for (a) Y20_MOD and (b) Y21_CTRL.

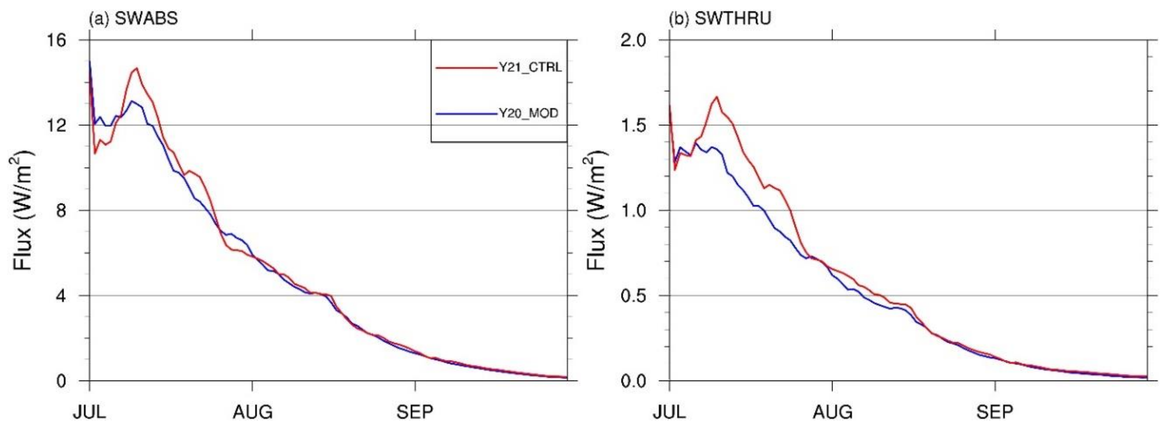

Figure ~~5, but for downward~~7 Time-series of (a) shortwave radiation ~~at the surface.~~absorbed by ice surface, and (b) penetrating shortwave radiation to the upper ocean averaged over ice-covered grid cells for Y20_MOD (blue line) and Y21_CTRL (red line).

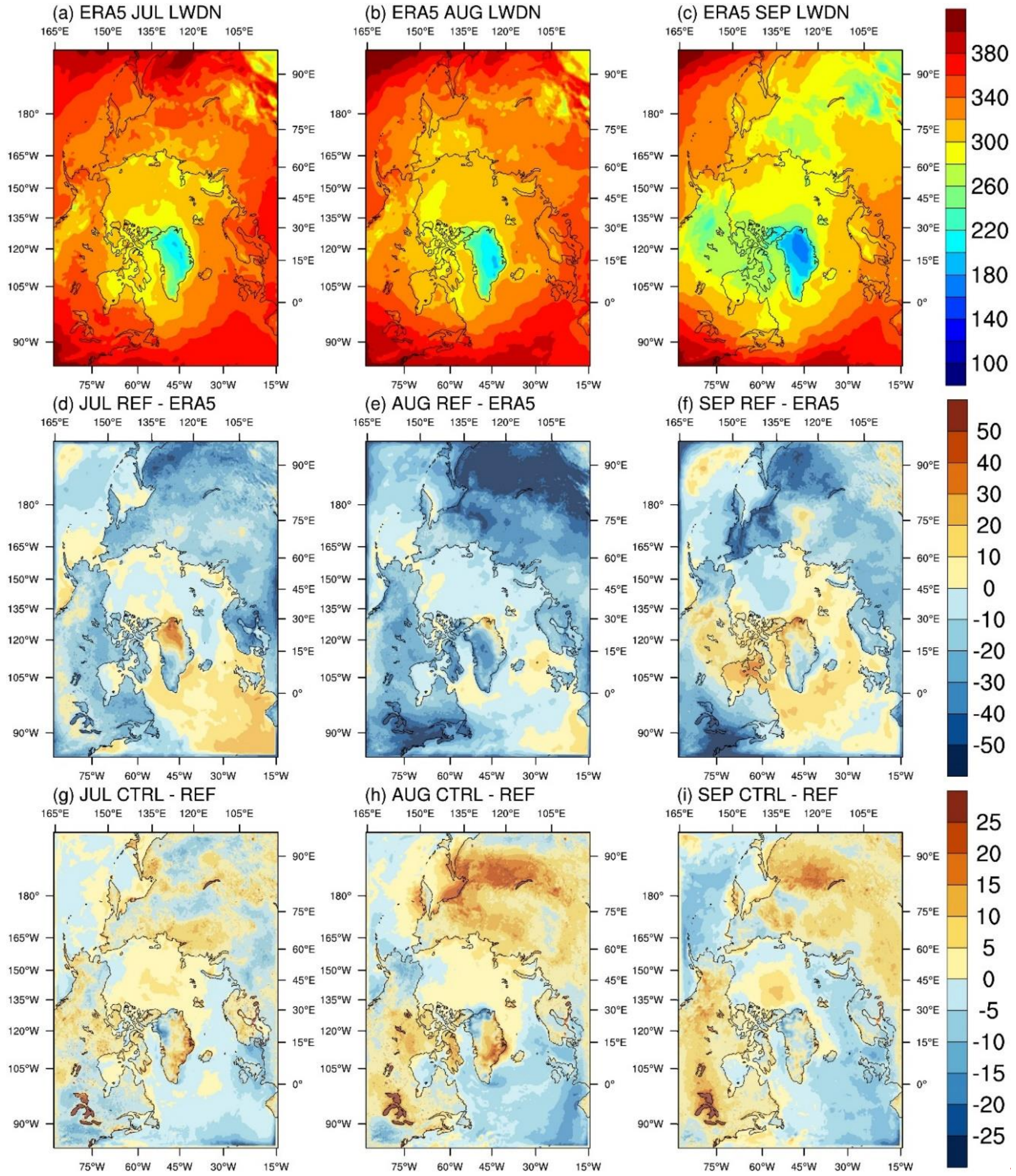

~~Figure 7 Same as Figure 6, but for downward thermal radiation at the surface.~~

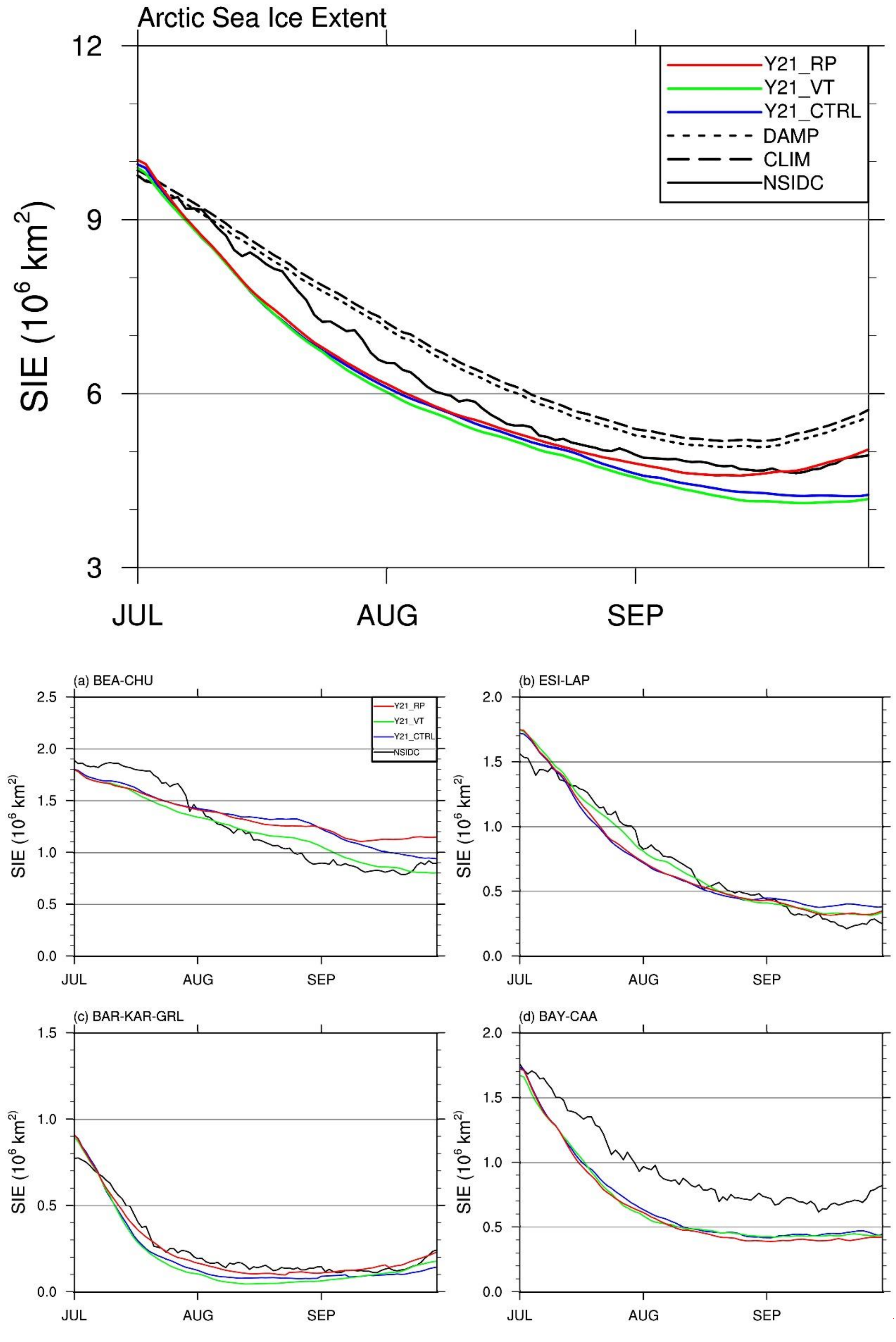
Arctic Sea Ice Extent
Y21_RP
Y21_VT
Y21_CTRL
DAMP
CLIM
NSIDC
SIE (10^6 km^2)
12
9
6
3
JUL
AUG
SEP
(a) BEA-CHU
(b) ESI-LAP
(c) BAR-KAR-GRL
(d) BAY-CAA
2.5
2.0
1.5
1.0
0.5
0.0

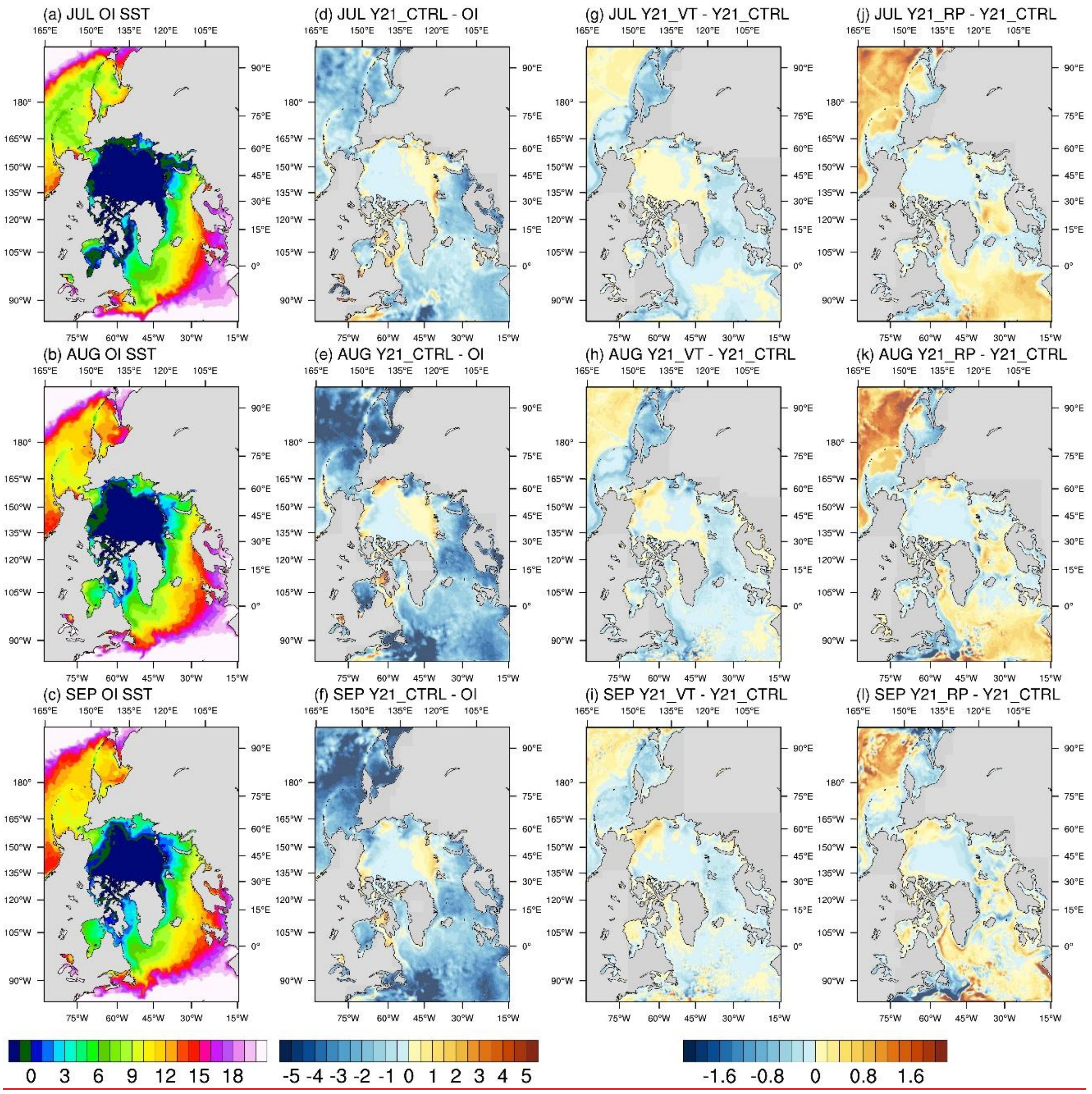

Figure 8 ~~Same as Figure 3, but for Y21_CTRL (blue line), Y21_VT (green line), and Y21_RP (red line).~~

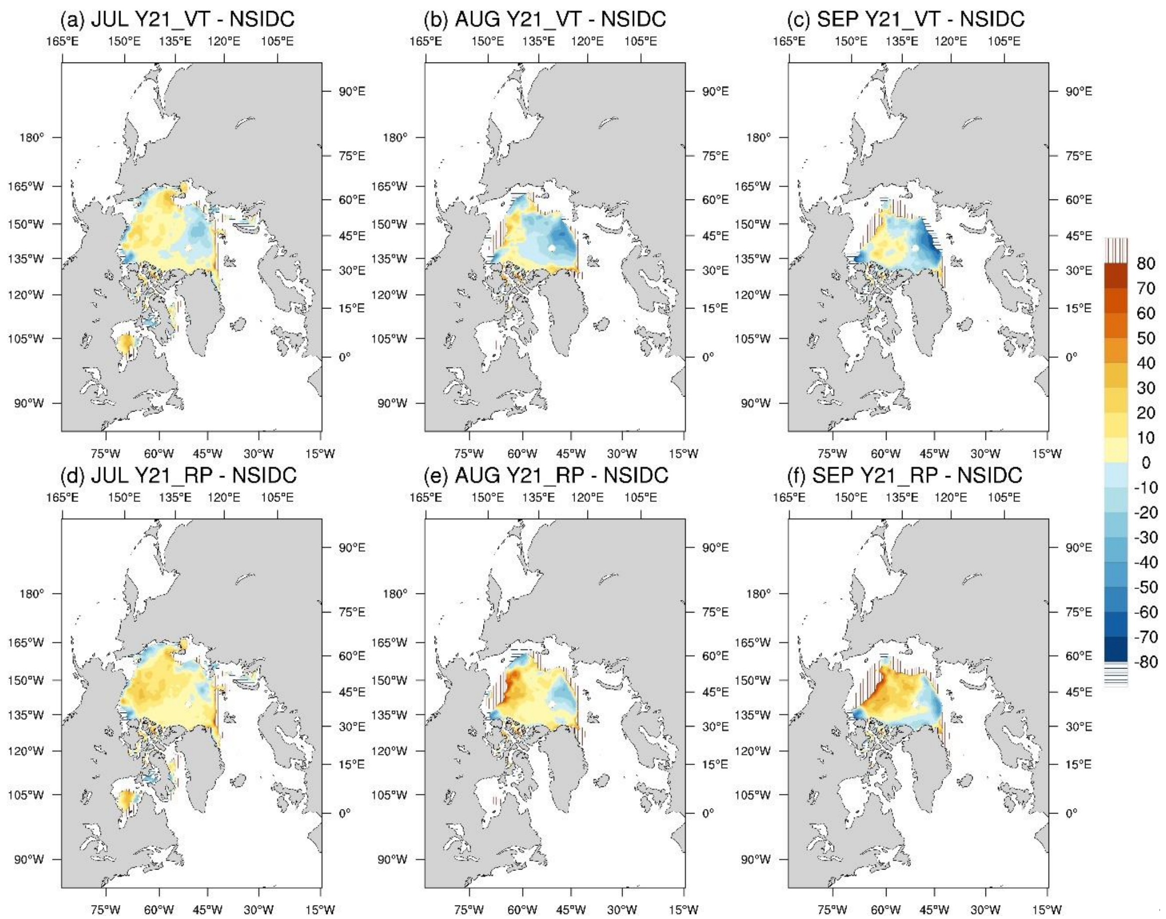

~~Figure 9 Monthly mean of sea ice concentration difference between the predictions and the observations for (a) July, (b) August, (c) September of Y21_VT, (d) July, (e) August, and (f) September of Y21_RP. Vertical/horizontal line areas represent the difference of ice edge location (15% concentration).~~

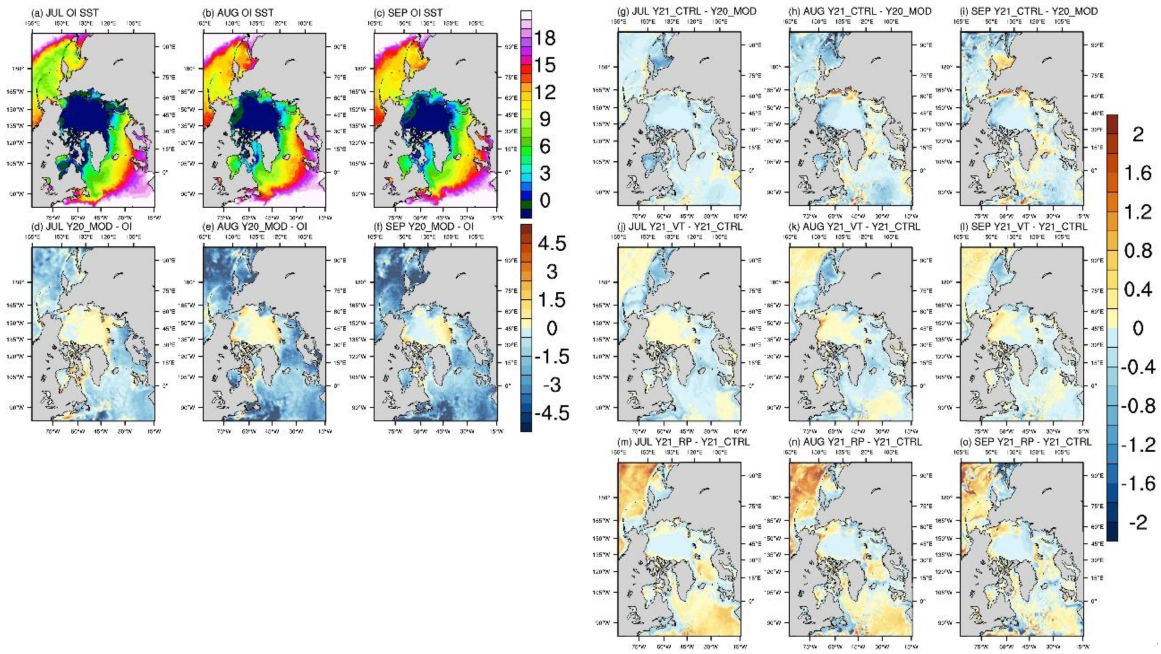

~~Figure 10 Left panel: Monthly~~First column: monthly mean of sea surface temperature for (a) July, (b) August, (c) September of the OI SST~~, and~~. Second column: the difference between ~~the predictions~~Y21_CTRL and the ~~observations~~OI SST for (d) July, (e) August, (f) September ~~of Y20_MOD~~. Right panel: Monthly mean of sea surface temperature difference between Y21_~~CTRL and Y20_MOD for (g) July, (h) August, (i) September, and the difference between Y21_VT~~VT/Y21_RP and Y21_CTRL for (g) July, (h) August, (i) September of Y21_VT, (j) July, (k) August, and (l) September of Y21_~~VT, (m) July, (n) August, and (o) September of Y21_RP.~~RP.

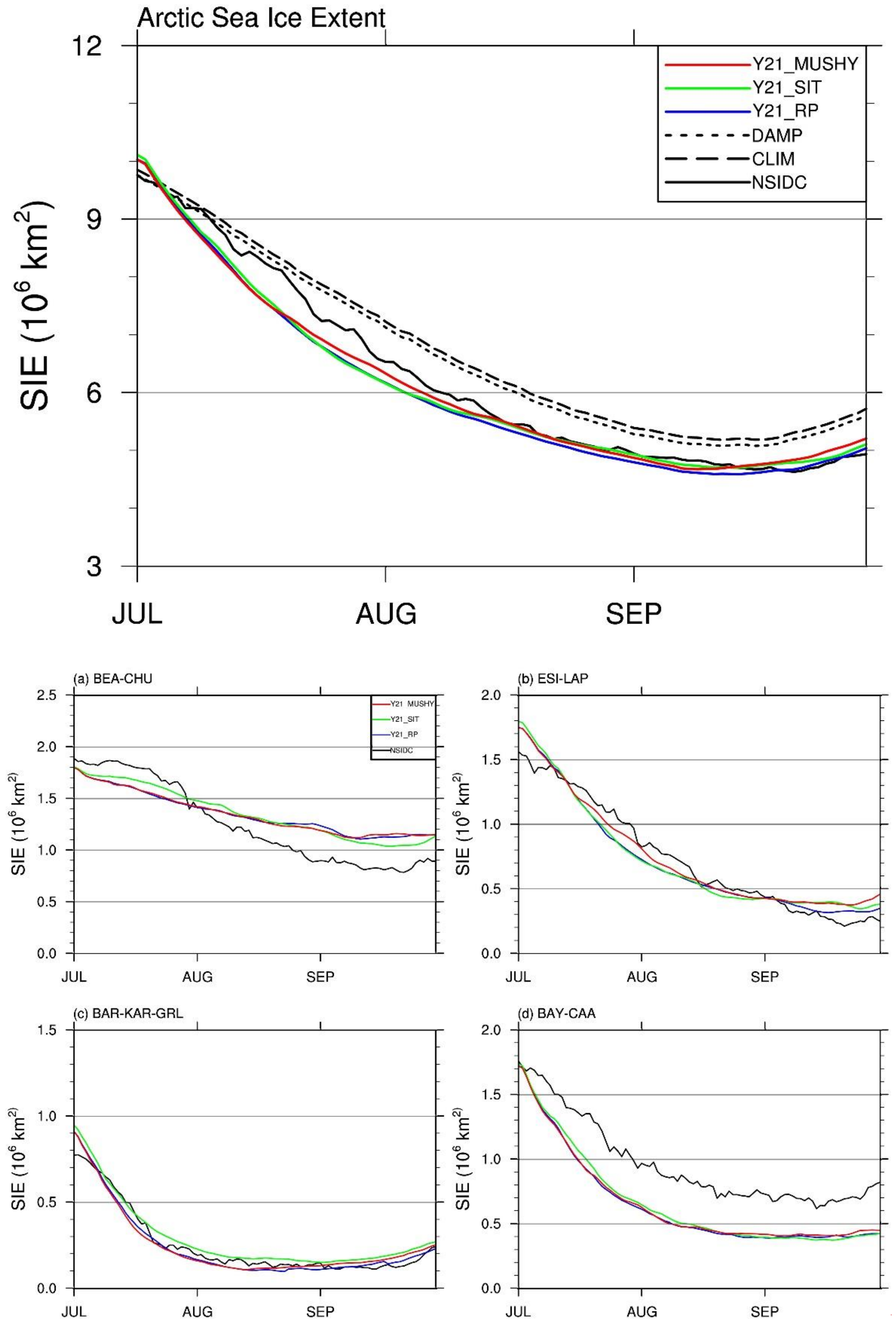
Arctic Sea Ice Extent
Y21_MUSHY
Y21_SIT
Y21_RP
DAMP
CLIM
NSIDC
SIE (10^6 km^2)
12
9
6
3
JUL
AUG
SEP
(a) BEA-CHU
(b) ESI-LAP
(c) BAR-KAR-GRL
(d) BAY-CAA
2.5
2.0
1.5
1.0
0.5
0.0

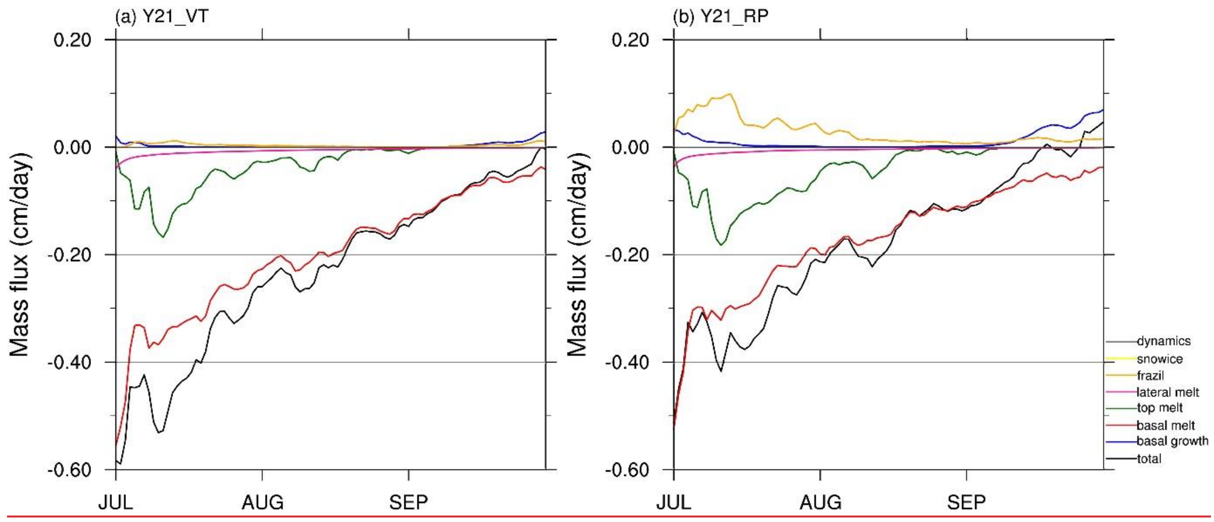

Figure 9 Same as Figure 6, but for (a) Y21_VT, and (b) Y21_RP.

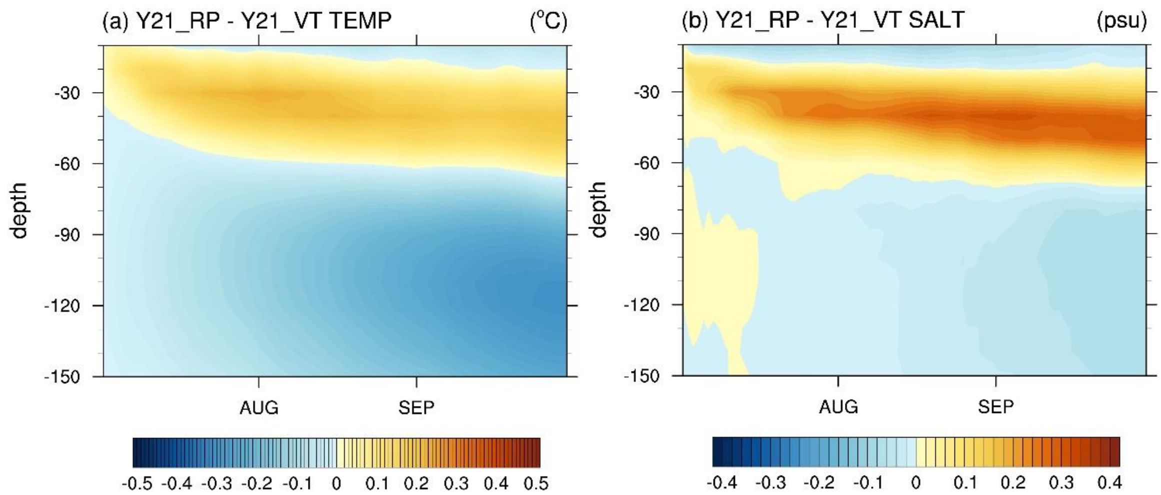

Figure 10 (a) the average temperature profile of upper 150 m under ice-covered areas for the difference between Y21_RP and Y21_VT. (b) same as (a), but for the salinity profile.

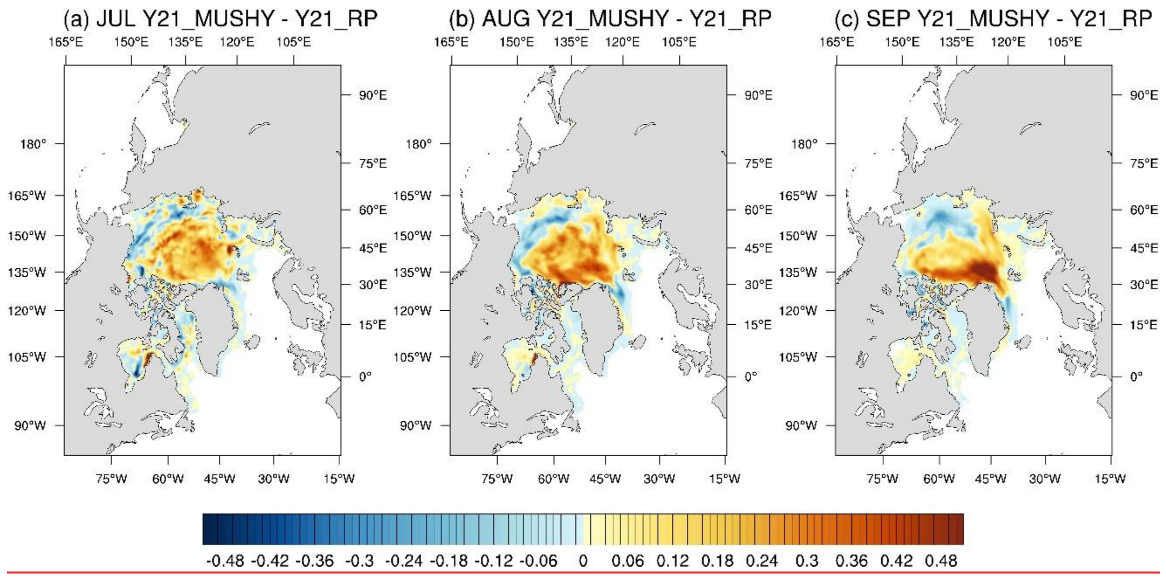

Figure 11 ~~Same as Figure 3, but for Y21_RP, Y21_MUSHY, and Y21_SIT.~~

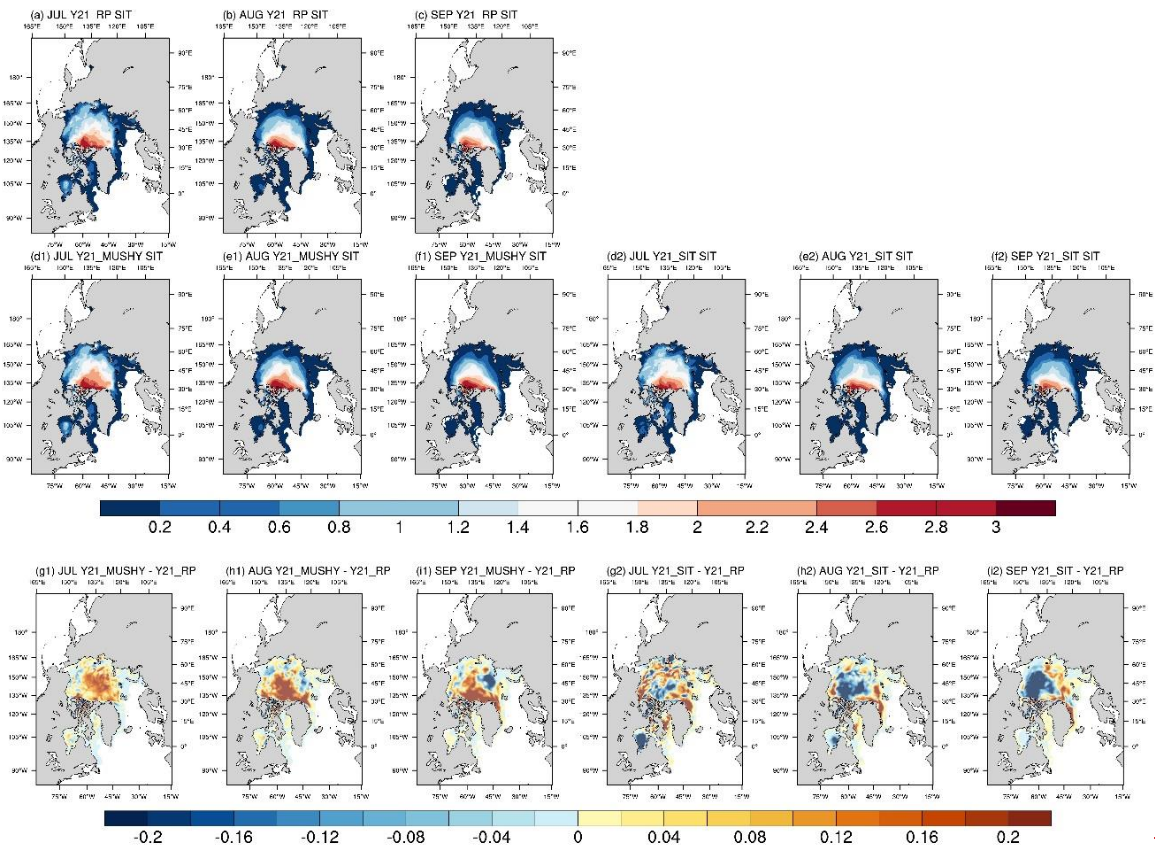

~~Figure 12~~ Monthly mean of sea ice thickness ~~for (a) July, (b) August, and (c) September of Y21_RP, (d_1) July, (e_1) August, (f_1) September of Y21_MUSHY, (d_2) July, (e_2) August, (f_2) September of Y21_SIT, the difference between Y21_MUSHY and Y21_RP for (g_1) July, (h_1) August, and (i_1) September, and the difference between Y21_SIT and Y21_RP for (g_2) July, (h_2) August, and (i_2) September.~~difference between Y21_MUSHY and Y21_RP for (a) July, (b) August, and (c) September.

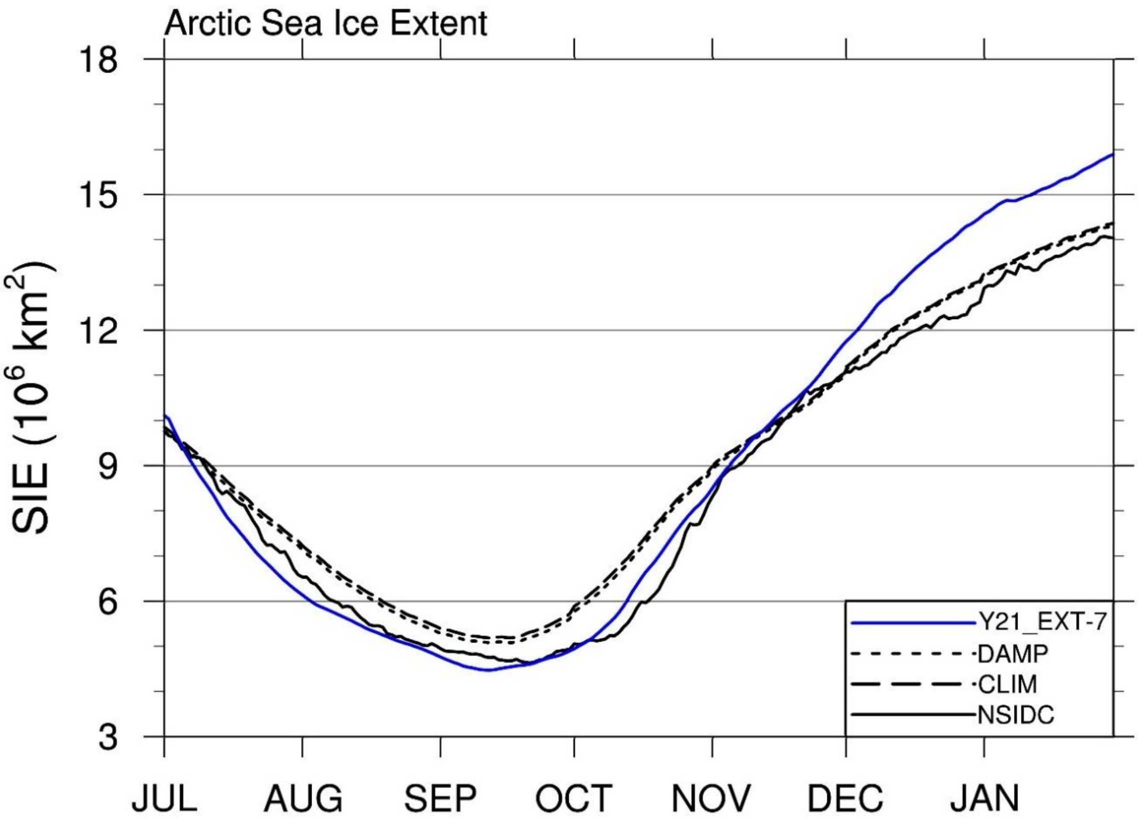
Arctic Sea Ice Extent
SIE (10^6 km^2)
18
15
12
9
6
3
JUL
AUG
SEP
OCT
NOV
DEC
JAN
Y21_EXT-7
DAMP
CLIM
NSIDC

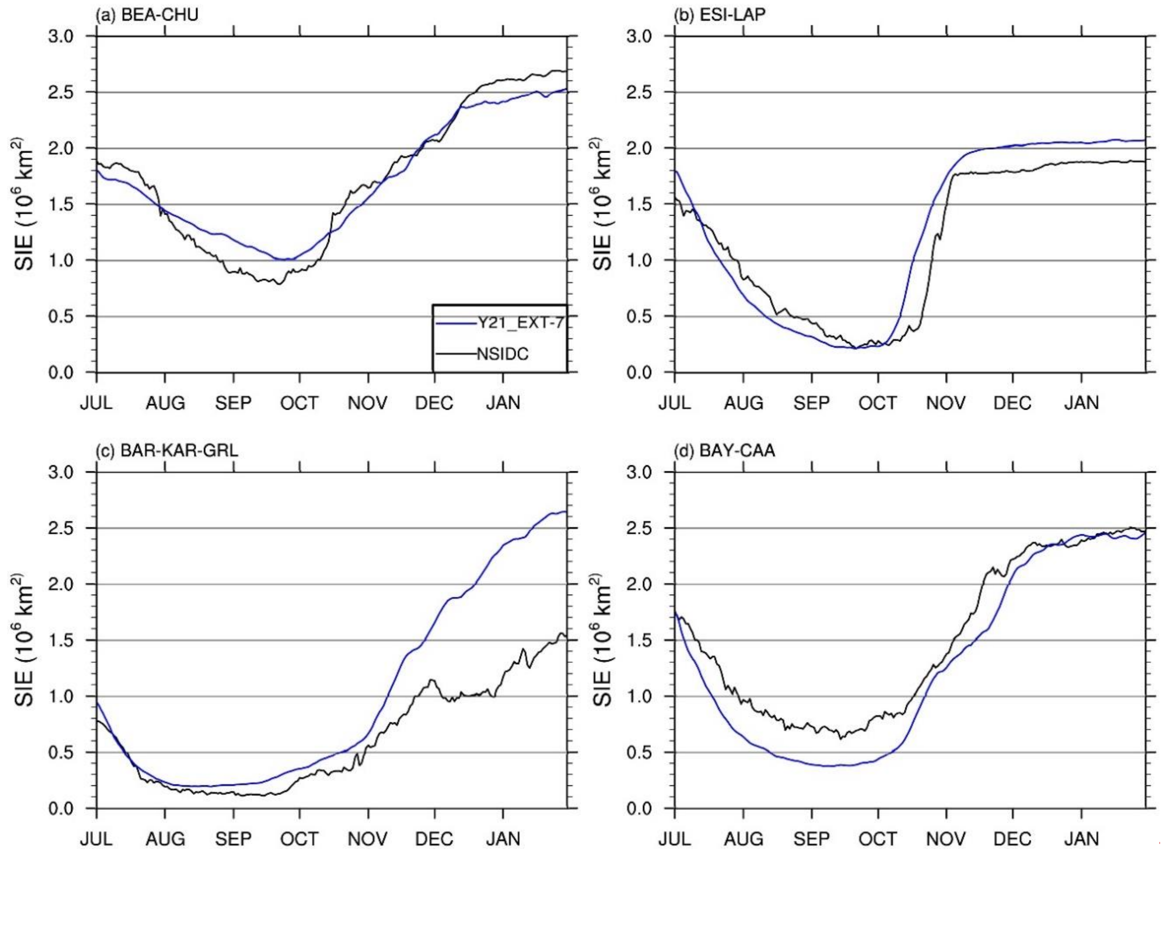
(a) BEA-CHU
(b) ESI-LAP
(c) BAR-KAR-GRL
(d) BAY-CAA
SIE (10^6 km^2)
3.0
2.5
2.0
1.5
1.0
0.5
0.0
JUL
AUG
SEP
OCT
NOV
DEC
JAN
Y21_EXT-7
NSIDC

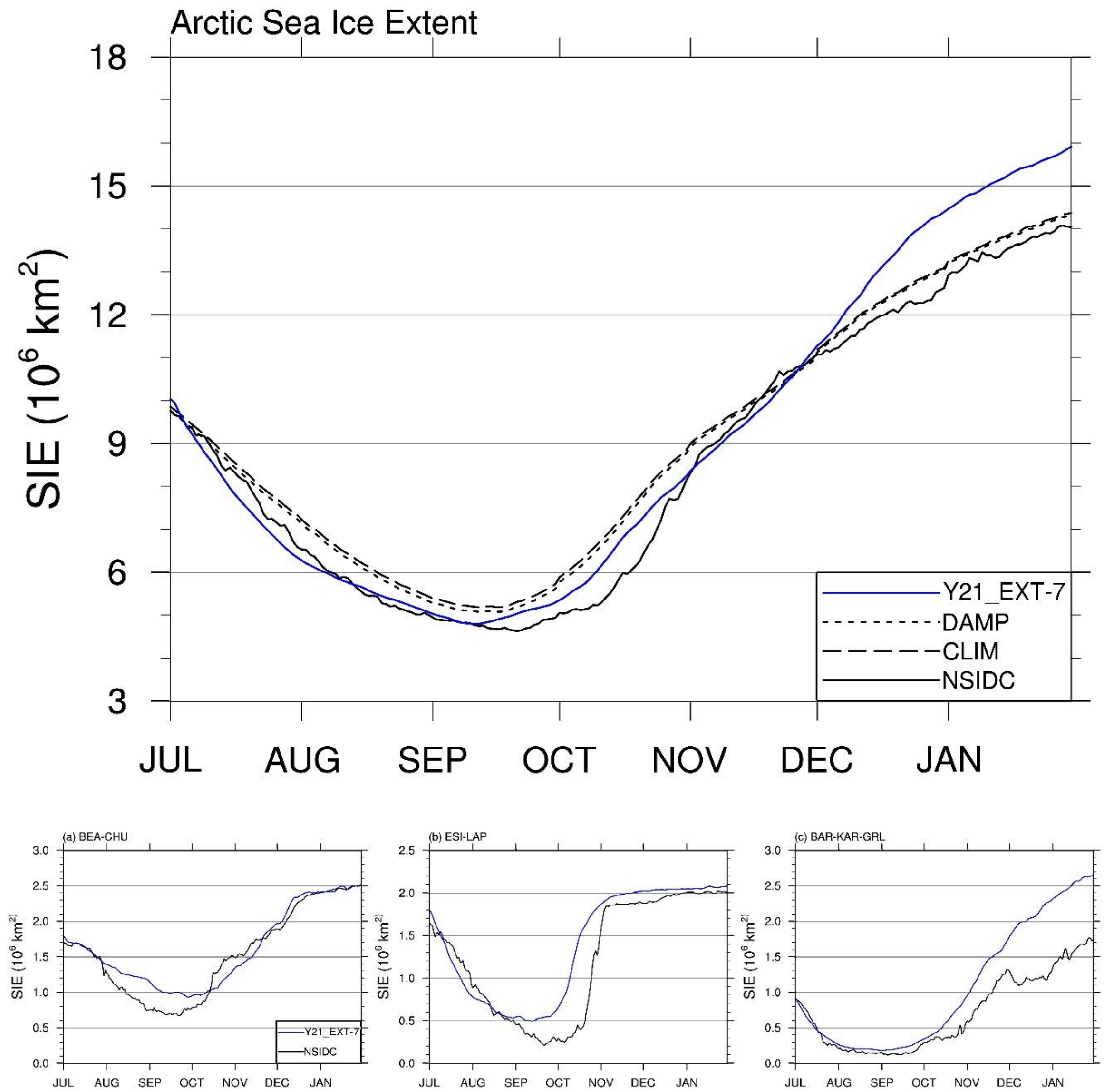

Figure 12 Same as Figure 4, but for Y21_EXT-7.

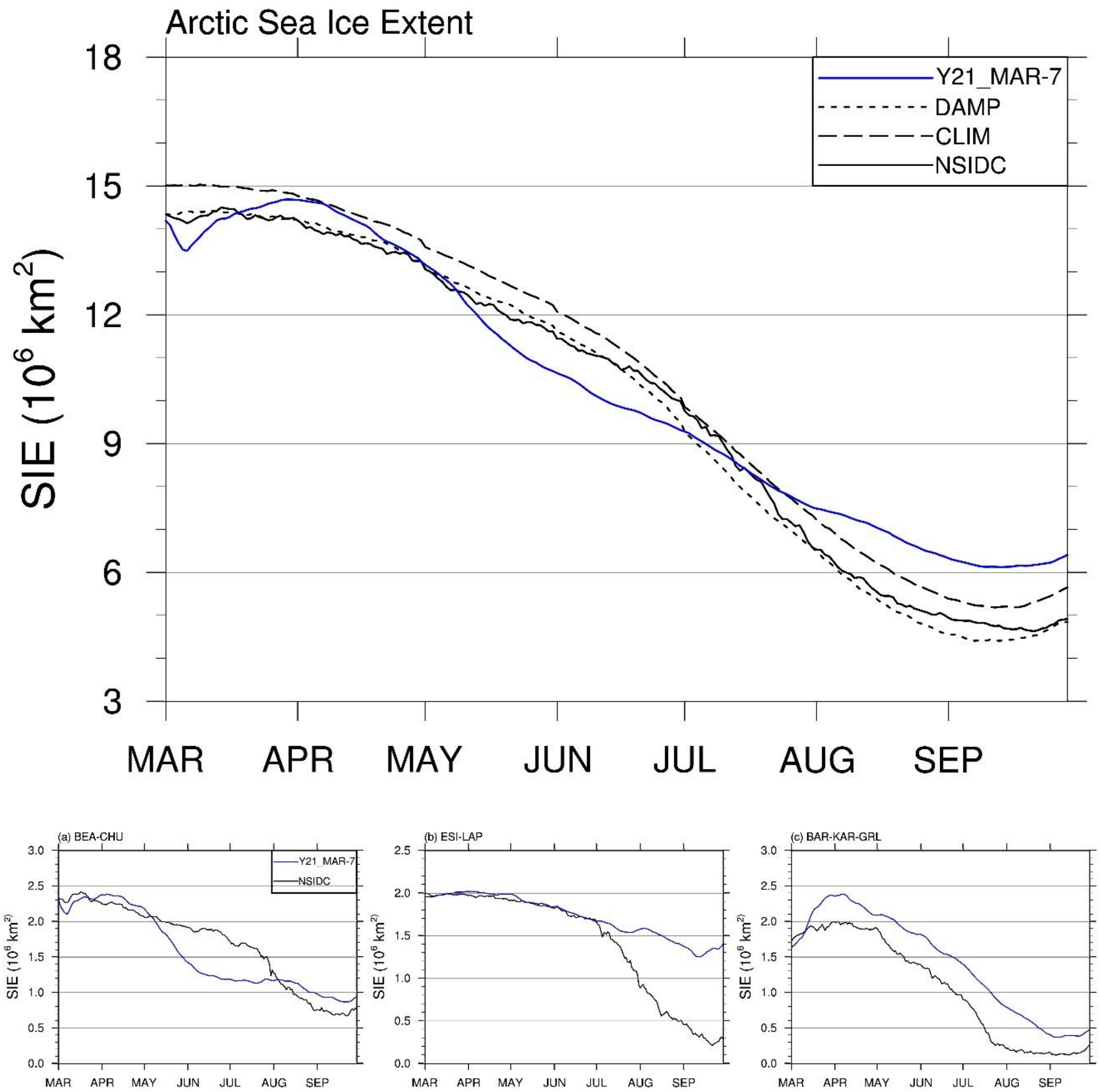

Figure 13 Same as Figure ~~3, but for Y21_EXT-7.~~

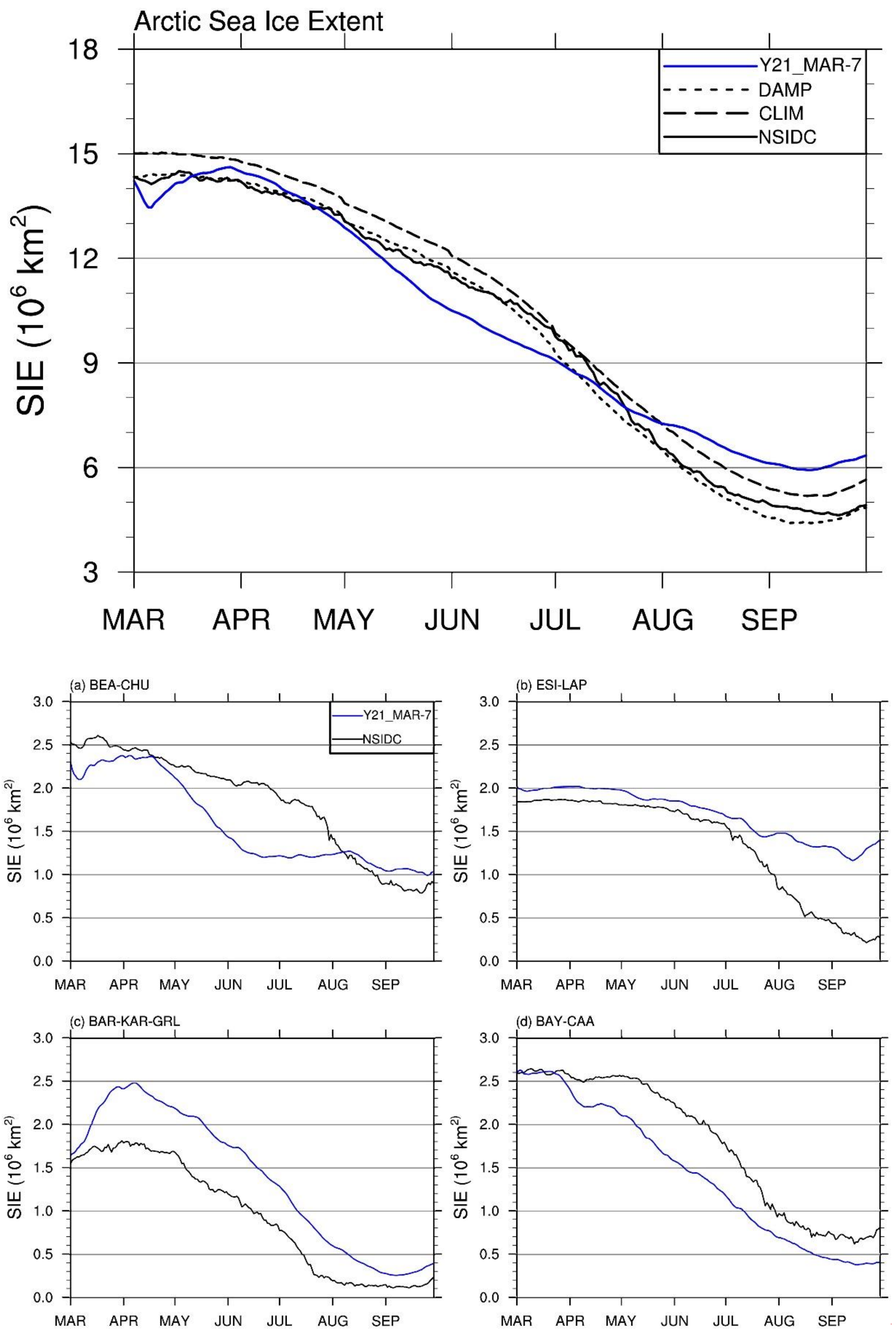

~~Figure 14 Same as Figure 3~~4, bur for Y21_MAR-7.

1330